

A shape reconstruction method for electromagnetic tomography using adjoint fields and level sets

Oliver Dorn* Eric L. Miller* Carey M. Rappaport *

March 20, 2000

Abstract

A two-step shape reconstruction method for electromagnetic (EM) tomography is presented which uses adjoint fields and level sets. The inhomogeneous background permittivity distribution and the values of the permittivities in some penetrable obstacles are assumed to be known, and the number, sizes, shapes, and locations of these obstacles have to be reconstructed given noisy limited-view EM data. The main application we address in the paper is the imaging and monitoring of pollutant plumes in environmental cleanup sites based on cross-borehole EM data. The first step of the reconstruction scheme makes use of an inverse scattering solver which first recovers equivalent scattering sources for a number of experiments, and then calculates from these an approximation for the permittivity distribution in the medium. The second step uses this result as an initial guess for solving the shape reconstruction problem. A key point in this second step is the fusion of the 'level set technique' for representing the shapes of the reconstructed obstacles, and an 'adjoint field technique' for solving the nonlinear inverse problem. In each step, a forward and an adjoint Helmholtz problem are solved based on the permittivity distribution which corresponds to the latest best guess for the representing level set function. A correction for this level set function is then calculated *directly* by combining the results of these two runs. Numerical experiments are presented which show that the derived method is able to recover one or more objects with nontrivial shapes given noisy cross-borehole EM data.

*Center for Electromagnetics Research, Northeastern University, Boston, MA, E-mail: dorn@cer.neu.edu, elmiller@ece.neu.edu, rappaport@neu.edu

Contents

1	Introduction	3
2	The physical experiment	6
2.1	The Helmholtz Equation	6
2.2	Formulation of the inverse problem	7
3	The shape reconstruction problem	8
3.1	Shape reconstruction and inverse scattering	8
3.2	The domains $\Omega^{(n)}$	9
3.3	Level set representation of the domains $\Omega^{(n)}$	10
4	Step 2: Solving the shape reconstruction problem	11
4.1	Function spaces	12
4.2	Operators	12
4.3	Linearized operators	14
4.4	A nonlinear Kaczmarz-type approach	15
4.5	The minimization problem	16
4.6	The adjoint linearized operators	17
4.7	The operators $T'_{jk}T'^{*}_{jk}$	18
4.8	Regularization of $T'_{jk}T'^{*}_{jk}$	18
4.9	Updating the level set function	20
4.10	Implementation: The levelART algorithm	22
5	Step 1: A Source-Type Adjoint Field method	23
5.1	Source-type methods	24
5.2	Solving the inverse scattering problem	25
5.3	Looking for a scattering source	26
5.4	Recovery of the scattering potential	28
5.5	Combining the results from single experiments	29
5.6	The initial level set function	30
5.7	Implementation: The STAF algorithm	31
6	Numerical Experiments	31
6.1	Discretization of the computational domain.	31
6.2	A full-view example	33
6.3	A cross-borehole situation with multiple objects	34
6.4	A cross-borehole situation with a single inclusion and variable conductivity	36

7	Summary and future directions	37
8	Acknowledgments	39
9	Appendix	39
9.1	Proof of theorem 5.1	39
9.2	Proof of theorem 5.2	40
10	Figures	43

1 Introduction

In this paper, we investigate the retrieval of an unknown number of penetrable objects (inclusions) imbedded in an inhomogeneous background medium based on observations of electromagnetic (EM) fields. The electromagnetic characteristics (permittivity and conductivity) of the background medium as well as of the material forming the inclusions are assumed to be known, but the main topological information concerning the number, sizes, shapes, and locations of the inclusions is missing and has to be reconstructed from the EM data.

One possible technique for using EM fields in cross-borehole tomography is ElectroMagnetic Induction Tomography (EMIT) [3, 18, 44, 49, 50, 51] which typically operates at frequencies between 1 to 20 kHz. In this frequency band, electromagnetic fields tend to diffuse rather than propagate as waves through the Earth. Penetration depths of 100 m or more are possible at these low frequencies, but the diffusional behavior of the fields makes the inverse problem severely ill-posed.

However, if the typical distances in the area of interest are not much larger than 10-20 m, we can use EM fields in the higher frequency band of 5 to 30 MHz instead. The wavelengths of these fields are typically between 2-15 m in moist soil, where the relative dielectric constant is typically around 20 [48]. Therefore, we can make use of wave propagation phenomena in the inversion process. In the present paper, we address this situation. The main application we have in mind is the imaging and monitoring of pollutant plumes at environmental cleanup sites given cross-borehole EM data, where the distances of the boreholes are not much larger than 10-20 m.

We assume that the known conductivity distribution is positive but small everywhere, and that the permittivity distribution in the medium has to be recovered. Inside the pollutant plumes, the permittivity is assumed to be constant with a known value, and the background permittivity is arbitrary but also known. Therefore, the task is to find the *number, shapes, sizes and locations of the pollutant plumes* from cross-borehole data gathered for a small number (less than 10) of frequencies. No

topological constraints are made on the shapes of these plumes. For example, they are allowed to be multiply connected, and to enclose 'cavities' or 'holes' filled with background material.

The main difficulties which arise in this situation are 1.) We want to allow for an (arbitrary) inhomogeneous background permittivity distribution in the inversion; 2.) The inverse problem is usually strongly nonlinear because of the high contrast of the permittivity values inside the plumes to the background medium; 3.) The data in our application are typically noisy and have only limited view; and 4.) The number of the plumes is typically unknown, and their shapes can have a complicated geometry.

In this paper, we propose a new shape reconstruction method which works in a two-step fashion in order to overcome these difficulties.

The first step of this combined inversion scheme plays the role of an initializing procedure for the second step, and employs a 'source-type' inversion method (which is described in more details in section 5) to deal with the high nonlinearity in the problem due to the presence of strong scatterers.

Then, the second step directly starts with the outcome of this initializing procedure, and continues by using a combination of the 'adjoint field technique' and a level set representation of the shapes until the inversion task is completed. Using a level set representation in this second step enables us to easily describe and keep track of complicated geometries which arise during the inversion process.

Both steps use an 'adjoint field technique' for the inversion which has the very useful property that the inverse problem can be solved approximately by making two uses of the same forward modelling code. Using a somewhat oversimplified description of our technique, the updates to the level set function are obtained by first making one pass through the code using the permittivity distribution corresponding to the latest best guess of the level set function, and then another pass with the adjoint operator applied to the differences in computed and measured data. Then the results of these two calculations are combined to determine updates to the level set function. The resulting procedure is iterative, and can be applied successively to parts of the data, e.g., data associated with one transmitter location and one frequency can be used to update the model before other transmitter locations and other frequencies are considered. This general procedure has several of the same advantages as wave equation migration in reflection seismology [10] and is also related to recent methods in EM migration introduced in Zhdanov *et al.* [51]. A similar technique has been successfully applied recently as part of an iterative nonlinear inversion scheme in [17, 18, 33].

The *level set method* was originally developed by Osher and Sethian for describ-

ing the motion of curves and surfaces [35, 41]. Since then, it has found applications in a variety of quite different situations. Examples are image enhancement, computer vision, interface problems, crystal growth, or etching and deposition in the microchip fabrication. For an overview we refer to [42].

The idea of using a level set representation as part of a solution scheme for inverse problems involving obstacles was first suggested by Santosa in [40]. More recently, a similar method was applied to a nonlinear inverse scattering problem by Litman *et al.* in [28]. In that work, an inverse transmission problem in free space is solved by a controlled evolution of a level set function. This evolution is governed by a Hamilton-Jacobi type equation, whose velocity function has to be determined properly in order to minimize a given cost functional.

The approach developed here does not lead to a Hamilton-Jacobi type equation. We follow an optimization approach, and employ a very specific inversion routine (an adjoint field technique) for solving it. This has the advantage that we do not have to propagate the level set function explicitly by computing a numerical Hamiltonian. Instead, our inversion routine provides us in each step with an update that has to be applied *directly* to the most recent level set function. Doing so, we automatically 'propagate' the level set function until the method converges.

This gain in simplicity, however, has its price. In order to arrive at an efficient scheme which is practically useful as well as easy to implement, we will apply some suitable approximations when deriving the algorithm. We will point out and discuss these approximations in those sections of the paper where they are applied.

For interesting approaches to solving shape recovery problems in various applications we refer to [23, 24, 26] and to the references therein. For alternative approaches to the shape reconstruction method in geophysical applications see [30, 39, 43] and the references therein. The treatment of more general inverse scattering problems is for example addressed in [4, 8, 11, 12, 15, 22, 31, 33, 38].

The paper is organized as follows. In section 2 we will present the basic equations of 2D EMs in a form convenient for development of the shape reconstruction technique. In section 3 we formulate the shape reconstruction problem and introduce the level set formulation of this problem. In section 4, we derive the basic shape reconstruction algorithm using level sets and adjoint fields. Section 5 describes how to calculate a suitable initialization for the shape reconstruction algorithm. In Section 6 numerical experiments are presented which demonstrate the performance of the algorithm in different situations. The final section summarizes the results of this paper and indicates some directions for future research.

2 The physical experiment

2.1 The Helmholtz Equation

We consider the 2D Helmholtz Equation

$$\Delta u + k^2(x)u = q(x) \quad \text{in } \mathbf{R}^2, \quad (1)$$

with complex wavenumber

$$k^2(x) = \omega^2 \mu_0 \epsilon_0 \left[\epsilon(x) + i \frac{\sigma(x)}{\omega \epsilon_0} \right]. \quad (2)$$

Here, $i^2 = -1$, ω denotes the angular frequency $\omega = 2\pi f$, μ_0 is the magnetic permeability in free space $\mu_0 = 4\pi \times 10^{-7}$ Henrys per meter, ϵ_0 is the dielectric permittivity in free space $\epsilon_0 = 8.854 \times 10^{-12}$ Farads per meter, ϵ is the relative dielectric permittivity (dimensionless), and σ is the electric conductivity in Siemens per meter. The form of (2) corresponds to time-harmonic line sources $\tilde{q}(x, t)$ which have a time-dependence $\tilde{q}(x, t) = q(x)e^{-i\omega t}$. For these sources we require that there exists a radius $r_0 > 0$ such that $\text{supp}(q) \subset\subset B_{r_0}(0)$, where $B_r(x) = \{y \in \mathbf{R}^2, |x - y| < r\}$ denotes the open ball centered in x with radius $r > 0$. For simplicity we assume throughout the paper that we can find a ball $B_R(0)$ with $R > r$ such that the complex wavenumber $k^2(x)$ is constant with value k_0^2 in $\mathbf{R}^2 \setminus B_R(0)$, and that for this k_0 the field u generated by (1) satisfies the Sommerfeld radiation condition

$$\lim_{r \rightarrow \infty} \sqrt{r} \left(\frac{\partial u}{\partial r} - ik_0 u \right) = 0 \quad (3)$$

with $r = |x|$ where the limit is assumed to hold uniformly in all directions $x/|x|$. With this assumption, the problem (1)-(3) possesses a uniquely determined solution u in \mathbf{R}^2 [12].

Furthermore we will consider in this paper only the case that the conductivity is positive everywhere, $\sigma > 0$ in \mathbf{R}^2 , and that it is small in some sense which will be specified later. Typical values in our geophysical examples will be $\sigma \approx 10^{-3} - 10^{-4}$ Siemens per meter or less [48].

We want to introduce some notation here which will be useful in the following. We denote the wavenumber $k^2(x)$ in short form by

$$k^2(x) = \kappa(x) = a\epsilon(x) + ib\sigma(x), \quad a = \omega^2 \mu_0 \epsilon_0, \quad b = \omega \mu_0. \quad (4)$$

We only consider positive frequencies $\omega > 0$ such that $a, b > 0$.

2.2 Formulation of the inverse problem

We assume that we are given p different source distributions q_j , $j = 1, \dots, p$. For each of these sources, data are gathered at the detector positions x_d , $d = 1, \dots, D_j$, for various frequencies f_k , $k = 1, \dots, K$. The total number of receivers D_j , as well as their positions x_d , might vary with the source q_j . We assume, for simplicity in the notation, that these positions do not depend on the frequency f_k . This restriction is, however, not necessary for the derivation of the inversion method. We require that there exists a radius $r_1 > 0$ such that all receiver positions are inside the ball of radius r_1 , i.e. $x_{jd} \in B_{r_1}(0)$ for all $d = 1, \dots, D_j$, $j = 1, \dots, p$.

For a given source q_j and a given frequency f_k we collect a set of data \tilde{G}_{jk} which is described by

$$\tilde{G}_{jk} = \left(\tilde{u}_{jk}(x_{j1}), \dots, \tilde{u}_{jk}(x_{jd}), \dots, \tilde{u}_{jk}(x_{jD_j}) \right)^T \in Z_j \quad (5)$$

with $Z_j = \mathbb{C}^{D_j}$ being the data space corresponding to a single experiment using one source and one frequency only. In (5), the fields \tilde{u}_{jk} solve (1)-(3) with the correct permittivity distribution $\tilde{\epsilon}(x)$, i.e.

$$\Delta \tilde{u}_{jk} + [a_k \tilde{\epsilon}(x) + ib_k \sigma(x)] \tilde{u}_{jk} = q_j(x) \quad \text{in } \mathbb{R}^2 \quad (6)$$

with

$$a_k = \omega_k^2 \mu_0 \epsilon_0, \quad b_k = \omega_k \mu_0, \quad \omega_k = 2\pi f_k. \quad (7)$$

In a slightly more formal way, we define for a given source q_j the measurement operator M_j acting on solutions u of (1) by

$$M_j u = \left(\int_{\mathbb{R}^2} u(x) \delta(x - x_{jd}) dx \right)_{d=1, \dots, D_j}^T. \quad (8)$$

With this notation, (5) is written as

$$\tilde{G}_{jk} = M_j \tilde{u}_{jk}, \quad j = 1, \dots, p, \quad k = 1, \dots, K. \quad (9)$$

We gather these data sets $\tilde{G}_{j,k}$ for all sources q_j , $j = 1, \dots, p$, and all frequencies f_k , $k = 1, \dots, K$, and the aim is to recover from this collection of data sets

$$\tilde{G} = (\tilde{G}_{1,1}, \dots, \tilde{G}_{p,K})^T \quad (10)$$

the unknown parameter distribution $\tilde{\epsilon}(x)$ in the domain of interest.

In the application of *EM cross-borehole tomography*, the sources and receivers are typically situated in some boreholes, and the permittivity distribution ϵ (and/or the conductivity distribution σ) between these boreholes has to be recovered from

the gathered data. In the 2D geometry considered here, typical sources are time-harmonic line sources which can be modelled in (1) by

$$q_j(x) = J_j \delta(x - x_j), \quad j = 1, \dots, p, \quad (11)$$

where x_j denotes the 2D coordinates of the j -th line source, $j = 1, \dots, p$, and the complex number J_j is the strength of the source. We will use these sources in our numerical experiments in section 6.

3 The shape reconstruction problem

In this section we formulate the shape reconstruction problem which we want to solve, and cast it in a form which makes use of the level set representation of the domains.

3.1 Shape reconstruction and inverse scattering

To start with we introduce some terminology which we will use throughout the paper.

Definition 3.1 *Let us assume that we are given a constant $\hat{\epsilon} > 0$, an open ball $B_r(0) \subset \mathbb{R}^2$ with $r > \max(r_0, r_1) > 0$, and a bounded function $\epsilon_b : \mathbb{R}^2 \rightarrow \mathbb{R}$. We call a pair (Ω, ϵ) , which consists of a compact domain $\Omega \subset\subset B_r(0)$ and a bounded function $\epsilon : \mathbb{R}^2 \rightarrow \mathbb{R}$, admissible if we have*

$$\epsilon|_{\Omega} = \hat{\epsilon}, \quad \epsilon|_{\mathbb{R}^2 \setminus \Omega} = \epsilon_b|_{\mathbb{R}^2 \setminus \Omega}. \quad (12)$$

In other words, a pair (Ω, ϵ) is *admissible* if ϵ is equal to a preassigned constant value $\hat{\epsilon}$ inside of Ω , and equal to the preassigned *background permittivity* ϵ_b outside of Ω . The domain Ω is called the *scattering domain*.

Remark 3.1 *For an admissible pair (Ω, ϵ) , and for given $\hat{\epsilon}$, ϵ_b , the permittivity ϵ is uniquely determined by Ω .*

With this definition, we can now formulate the *shape reconstruction problem*.

Shape reconstruction problem. Let us assume that we are given a constant $\hat{\epsilon} > 0$, a bounded function $\epsilon_b : \mathbb{R}^2 \rightarrow \mathbb{R}$, and some data \tilde{G} as in (10). Find a domain $\tilde{\Omega}$ such that the admissible pair $(\tilde{\Omega}, \tilde{\epsilon})$ reproduces the data, i.e. (9) holds with \tilde{u}_{jk} given by (6) for $j = 1, \dots, p$, $k = 1, \dots, K$.

Using the same notation and assumptions as in definition 3.1, we want to formulate another inverse problem which we will call the *inverse scattering problem* and which will play an important part when solving the shape reconstruction problem.

Inverse Scattering Problem. Let us assume that we are given a bounded function $\epsilon_b : \mathbb{R}^2 \rightarrow \mathbb{R}$, and some data \tilde{G} as in (10). Find a bounded function $\tilde{\epsilon}_s : \mathbb{R}^2 \rightarrow \mathbb{R}$ with $\text{supp}(\epsilon_s) \subset\subset B_r(0)$ such that $\tilde{\epsilon} = \epsilon_b + \tilde{\epsilon}_s$ reproduces the data, i.e. (9) holds with \tilde{u}_{jk} given by (6) for $j = 1, \dots, p$, $k = 1, \dots, K$.

The inverse scattering problem gives rise to the following decomposition of ϵ in \mathbb{R}^2 .

Decomposition of $\epsilon(x)$:

$$(i) \quad \epsilon = \epsilon_b + \epsilon_s \quad \text{in } \mathbb{R}^2 \quad (13)$$

$$(ii) \quad \text{supp}(\epsilon_s) \subset\subset B_r(0). \quad (14)$$

In other words, the permittivity distribution ϵ is decomposed into the background distribution ϵ_b and the perturbation ϵ_s which is assumed to have compact support and which we will refer to as the *scattering potential* in the following.

Solving the shape reconstruction problem requires only to find the *shape* of the domain $\tilde{\Omega}$, since the function $\tilde{\epsilon}$ is then uniquely determined by (12). Solving the inverse scattering problem, on the other hand, amounts to finding the entire function $\tilde{\epsilon}_s$ from the given data, which is much harder to do. However, it will turn out that finding a good *approximate* solution of the inverse scattering problem is much easier to achieve and will provide us with an excellent initial guess for starting our shape reconstruction routine.

Definition 3.1 allows us to formulate a first version of the strategy which we want to use for solving the shape reconstruction problem.

Strategy for solving the shape reconstruction problem. Construct a series of admissible pairs $(\Omega^{(n)}, \epsilon^{(n)})$, $n = 0, 1, 2, \dots$, such that the misfit between the data (10) and the calculated data corresponding to $(\Omega^{(n)}, \epsilon^{(n)})$ decreases with increasing n , and ideally, i.e. in absence of noise, tends to zero in the limit $n \rightarrow \infty$. Use the *approximate* solution of the inverse scattering problem (i),(ii) to initialize this series by determining a good starting element $(\Omega^{(0)}, \epsilon^{(0)})$.

3.2 The domains $\Omega^{(n)}$

In our numerical examples, each of the domains $\Omega^{(n)}$ which we are looking for can be given as a collection of a finite number L_n of disjoint, compact subdomains $\Omega_l^{(n)}$,

$l = 1, \dots, L_n$, with

$$\Omega^{(n)} = \bigcup_{l=1}^{L_n} \Omega_l^{(n)}, \quad \Omega_l^{(n)} \cap \Omega_{l'}^{(n)} = \emptyset \quad \text{for } l \neq l'. \quad (15)$$

The shapes of these subdomains $\Omega_l^{(n)}$ can in principle be arbitrary. In particular, they are allowed to be multiply connected, and to enclose some 'cavities' or 'holes' filled with background material. Moreover, the number L_n of these subdomains might (and usually does) vary with the iteration number n . For the derivation of the inversion method, we assume that the boundaries $\partial\Omega_l^{(n)}$ of these domains are sufficiently smooth (e.g. C^1).

It is essential for the success and the efficiency of the reconstruction scheme to have a good and flexible way of keeping track of the shape evolution during the reconstruction process. The method we have chosen in our reconstruction algorithm is a *level set representation* of the shapes as it was suggested by Santosa [40]. This representation has the advantage that the level set functions, which are in principle only used for *representing* the shapes, can in a natural way be made part of the reconstruction scheme itself. Doing so, it is not necessary anymore to refer to the shapes of the domains until the reconstruction process is completed. The *final* shape is then recovered from the representing level set function easily. In the following we will discuss in a more formal way how this can be achieved.

3.3 Level set representation of the domains $\Omega^{(n)}$

Assume that we are given a domain $\Omega \subset\subset B_r(0)$. The characteristic function $\chi_\Omega : \mathbb{R}^2 \rightarrow \{0, 1\}$ is defined in the usual way as

$$\chi_\Omega(x) = \begin{cases} 1 & , \quad x \in \Omega \\ 0 & , \quad x \in \mathbb{R}^2 \setminus \Omega. \end{cases} \quad (16)$$

Definition 3.2 We call a function $\phi : \mathbb{R}^2 \rightarrow \mathbb{R}$ a level set representation of Ω if

$$\chi_\Omega(x) = \Psi_\phi(x) \quad \text{on } \mathbb{R}^2 \quad (17)$$

where $\Psi_\phi : \mathbb{R}^2 \rightarrow \{0, 1\}$ is defined as

$$\Psi_\phi(x) = \begin{cases} 1 & , \quad \phi(x) \leq 0 \\ 0 & , \quad \phi(x) > 0. \end{cases} \quad (18)$$

For each function $\phi : \mathbb{R}^2 \rightarrow \mathbb{R}$ there is a domain Ω associated with ϕ by (17),(18) which we call $\Omega[\phi]$. It is clear that different functions ϕ_1, ϕ_2 , $\phi_1 \neq \phi_2$, can be associated with the same domain $\Omega[\phi_1] = \Omega[\phi_2]$, but that different domains cannot have

the same level set representation. Therefore, we can use the level set representation for unambiguously specifying a domain Ω by any one of its associated level set functions.

The boundary $\Gamma = \partial\Omega[\phi]$ of a domain $\Omega[\phi]$, represented by the level set function ϕ , is defined as

$$\begin{aligned} \Gamma = \{x \in \mathbb{R}^2 : \quad & \text{for all } \epsilon > 0 \text{ we can find } x_1, x_2 \in B_\epsilon(x) \\ & \text{with } \phi(x_1) > 0 \text{ and } \phi(x_2) < 0\} \end{aligned} \quad (19)$$

Definition 3.3 *We call a triple (Ω, ϵ, ϕ) , which consists of a domain $\Omega \subset\subset B_r(0)$ and bounded functions $\epsilon, \phi : \mathbb{R}^2 \rightarrow \mathbb{R}$, admissible if the pair (Ω, ϵ) is admissible in the sense of definition 3.1, and ϕ is a valid level set representation of Ω .*

Remark 3.2 *For an admissible triple (Ω, ϵ, ϕ) , and for given $\hat{\epsilon}, \epsilon_b$, the pair (Ω, ϵ) is uniquely determined by ϕ .*

We use these definitions to reformulate our shape reconstruction problem.

Level set formulation of the shape reconstruction problem. Given a constant $\hat{\epsilon} > 0$, a background distribution ϵ_b , and some data \tilde{G} as in (10). Find a level set function $\tilde{\phi}$ such that the corresponding admissible triple $(\tilde{\Omega}, \tilde{\epsilon}, \tilde{\phi})$ reproduces the data, i.e. (9) holds with \tilde{u}_{jk} given by (6) for $j = 1, \dots, p$, $k = 1, \dots, K$.

The strategy for solving this shape reconstruction problem has to be reformulated, too. It reads now as follows.

Strategy for solving the reformulated shape reconstruction problem. Construct a series of admissible triples $(\Omega^{(n)}, \epsilon^{(n)}, \phi^{(n)})$, $n = 0, 1, 2, \dots$, such that the misfit between the data (10) and the calculated data corresponding to $(\Omega^{(n)}, \epsilon^{(n)}, \phi^{(n)})$ decreases with increasing n , and ideally, i.e. in absence of noise, tends to zero in the limit $n \rightarrow \infty$. *For finding this series we only have to keep track of $\epsilon^{(n)}$ and $\phi^{(n)}$, but not of $\Omega^{(n)}$.* The function $\epsilon^{(n)}$ is needed in each step for solving a forward problem (1), and a corresponding adjoint problem. The knowledge of $\phi^{(n)}$ is used in each step to determine $\epsilon^{(n)}$. The final level set function $\phi^{(N)}$, which satisfies some stopping criterion, is used to recover the final shape $\Omega^{(N)}$ via (17).

4 Step 2: Solving the shape reconstruction problem

In this section we derive the basic shape reconstruction method which uses adjoint fields and the level set representation introduced above. The initializing procedure ('Step 1') for this reconstruction routine will be discussed in section 5.

4.1 Function spaces

We want to specify now the function spaces which we will be working with. The main objective of this section is to introduce the inner products on these function spaces, which will become important when defining the adjoint linearized operators in sections 4.6 and 5.3.

The space of sources and scattering sources Y is defined as

$$Y = \left\{ q : \mathbb{R}^2 \rightarrow \mathbb{C}, \quad q = 0 \text{ on } \mathbb{R}^2 \setminus B_r(0), \quad \int_{B_r(0)} |q|^2 dx < \infty \right\}, \quad (20)$$

$$\langle q_1, q_2 \rangle_Y = \int_{B_r(0)} q_1(x) \overline{q_2(x)} dx, \quad (21)$$

where the bar means 'complex conjugate'. The space F of scattering potentials is defined as

$$F = \left\{ \epsilon_s : \mathbb{R}^2 \rightarrow \mathbb{R}, \quad \epsilon_s = 0 \text{ on } \mathbb{R}^2 \setminus B_r(0), \quad \int_{B_r(0)} |\epsilon_s|^2 dx < \infty \right\}, \quad (22)$$

$$\langle \epsilon_{s,1}, \epsilon_{s,2} \rangle_F = \int_{B_r(0)} \gamma \epsilon_{s,1}(x) \epsilon_{s,2}(x) dx, \quad (23)$$

with some positive weighting factor $\gamma > 0$ which is introduced here for convenience. Analogously, the space of level set functions Φ is defined as

$$\Phi = \left\{ \phi : \mathbb{R}^2 \rightarrow \mathbb{R}, \quad \phi = 0 \text{ on } \mathbb{R}^2 \setminus B_r(0), \quad \int_{B_r(0)} |\phi|^2 dx < \infty \right\}, \quad (24)$$

$$\langle \phi_1, \phi_2 \rangle_\Phi = \int_{B_r(0)} \gamma \phi_1(x) \phi_2(x) dx. \quad (25)$$

This space for the level set functions is mainly chosen in order to have an inner product available which is convenient for the derivation of the shape reconstruction algorithm. We mention that the regularity of an arbitrary function in Φ is, strictly speaking, not sufficient for our purposes, such that we will apply further regularity constraints on those level set functions $\phi \in \Phi$ which we choose for representing the boundaries $\partial\Omega[\phi]$.

The data space Z_j corresponding to source q_j , $j = 1, \dots, p$, was already introduced earlier, and is given by $Z_j = \mathbb{C}^{D_j}$, where D_j is the total number of receivers corresponding to source q_j .

4.2 Operators

In the following, we will introduce some operators which will enable us to formulate the shape reconstruction problem in a way suitable for deriving the inversion algorithm.

Given a constant $\hat{\epsilon}$ and a bounded function $\epsilon_b : \mathbb{R}^2 \rightarrow \mathbb{R}$. Then, with each level set function $\phi \in \Phi$ a uniquely determined scattering potential $\Lambda(\phi)$ is associated by putting

$$\Lambda(\phi)(x) = \begin{cases} \hat{\epsilon} - \epsilon_b(x) & , \quad \phi(x) \leq 0 \\ 0 & , \quad \phi(x) > 0. \end{cases} \quad (26)$$

With (18) we can write this also as

$$\Lambda(\phi)(x) = \Psi_\phi(x)(\hat{\epsilon} - \epsilon_b(x)) \quad , \quad x \in \mathbb{R}^2. \quad (27)$$

Notice that the operator Λ is chosen such that the triple (Ω, ϵ, ϕ) with $\epsilon = \epsilon_b + \Lambda(\phi)$ and domain $\Omega[\phi]$ forms an admissible triple (Ω, ϵ, ϕ) in the sense of definition 3.3. Moreover, for (Ω, ϵ, ϕ) an admissible triple, we see that $\Lambda(\phi)$ is just the scattering potential ϵ_s as defined in (13),(14)

$$\Lambda(\phi)(x) = \epsilon_s(x) = \chi_\Omega(x)(\hat{\epsilon} - \epsilon_b(x)) \quad , \quad x \in \mathbb{R}^2. \quad (28)$$

Let us assume now that we are given a background permittivity ϵ_b and that we have collected some data \tilde{G}_{jk} which correspond to the 'true' permittivity distribution

$$\tilde{\epsilon} = \epsilon_b + \tilde{\epsilon}_s, \quad (29)$$

where $\tilde{\epsilon}_s$ is the 'true' scattering potential. The *residual operators* R_{jk} map for a source position q_j and a frequency f_k a given scattering potential ϵ_s to the corresponding mismatch in the data

$$R_{jk} : F \longrightarrow Z_j \quad , \quad R_{jk}(\epsilon_s) = M_j u_{jk} - \tilde{G}_{jk} \quad (30)$$

where u_{jk} solves

$$\Delta u_{jk} + [a_k(\epsilon_b + \epsilon_s)(x) + ib\sigma(x)] u_{jk} = q_j \quad (31)$$

and M_j is the measurement operator defined in (8). From (9) we see that for the 'true' scattering potential the residuals vanish,

$$R_{jk}(\tilde{\epsilon}_s) = 0 \quad \text{for } j = 1, \dots, p, \quad k = 1, \dots, K, \quad (32)$$

if the data are noise-free.

The *forward operators* T_{jk} which map a given level set function $\phi \in \Phi$ into the corresponding mismatch in the data are defined by

$$T_{jk} : \Phi \longrightarrow Z_j \quad , \quad T_{jk}(\phi) = R_{jk}(\Lambda(\phi)) \quad (33)$$

for $j = 1, \dots, p, \quad k = 1, \dots, K$. The goal is to find a level set function $\tilde{\phi} \in \Phi$ such that

$$T_{jk}(\tilde{\phi}) = 0 \quad \text{for } j = 1, \dots, p, \quad k = 1, \dots, K. \quad (34)$$

We mention that all three operators Λ , R_{jk} and T_{jk} are nonlinear.

4.3 Linearized operators

For the derivation of the shape reconstruction algorithm, we will need expressions for the linearized operators corresponding to the nonlinear operators introduced above, and for their adjoints with respect to the given inner products. In this section, we define the linearized operators, and expressions for their adjoints are derived in section 4.6.

In Santosa [40] it is shown that, for a homogeneous background ϵ_b , the infinitesimal response $\delta\epsilon_s(x)$ in the scattering potential $\epsilon_s(x)$ to an infinitesimal change $\delta\phi(x)$ of the level set function $\phi(x)$ has the form

$$\delta\epsilon_s(x) = - [\hat{\epsilon} - \epsilon_b] \frac{\delta\phi(x)}{|\nabla\phi(x)|} \Big|_{x \in \partial\Omega[\phi]}. \quad (35)$$

The function $\delta\epsilon_s$ in (35) can be interpreted as a 'surface measure' on the boundary $\Gamma = \partial\Omega[\phi]$. Similar to (35), we would like to define the linearized operator $\tilde{\Lambda}'[\phi]$ by

$$\left(\tilde{\Lambda}'[\phi] \delta\phi \right) (x) = - [\hat{\epsilon} - \epsilon_b(x)] \frac{\delta\phi(x)}{|\nabla\phi(x)|} \hat{\delta}_\Gamma(x) \quad (36)$$

where $\hat{\delta}_\Gamma(x)$ denotes the Dirac delta distribution concentrated on $\Gamma = \partial\Omega[\phi]$. In this interpretation, (36) describes an infinitesimal 'surface load' of permittivity on Γ which has to be recovered from the mismatch in the data.

However, the expression on the right hand side of (36) is not an element of F which causes problems when we want to calculate the inner products defined in section 4.1. Therefore, we will introduce an approximation to the operator (36) which maps from Φ into F and which will be more convenient for the derivation of the reconstruction method.

For a given level set function $\phi \in \Phi$, let $\Gamma = \partial\Omega[\phi]$ and $B_\rho(\Gamma) = \cup_{y \in \Gamma} B_\rho(y)$ a small neighborhood of Γ with some given constant $0 < \rho \ll 1$. The (approximated) linearized operator $\Lambda'[\phi]$ is defined as

$$\Lambda'[\phi] : \Phi \longrightarrow F, \quad (\Lambda'[\phi] \delta\phi) (x) = - [\hat{\epsilon} - \epsilon_b(x)] \frac{\delta\phi(x)}{|\nabla\phi(x)|} C_\rho(\Gamma) \chi_{B_\rho(\Gamma)}(x). \quad (37)$$

Here, $C_\rho(\Gamma) = L(\Gamma)/\text{Vol}(B_\rho(\Gamma))$ where $L(\Gamma) = \int_{B_r(0)} \hat{\delta}_\Gamma(x) dx$ is the length of the boundary Γ , and $\text{Vol}(B_\rho(\Gamma)) = \int_{B_r(0)} \chi_{B_\rho(\Gamma)}(x) dx$ is the volume of $B_\rho(\Gamma)$. For a very small ρ we will get a very large weight $C_\rho(\Gamma)$, whereas for increasing ρ this weight $C_\rho(\Gamma)$ decreases accordingly. The operator defined in (37) maps now from Φ into F such that we can make use of the inner products defined on these spaces.

We mention that the term $|\nabla\phi(x)|$ in (35), (36), as well as the derivation of these expressions, implies some regularity constraint on ϕ . For example, $\phi \in C^1$ would be possible. Another possibility would be to use a 'signed distance function'

as a standard representation of the boundary [42]. We do not want to specify the regularity of ϕ at this point, but assume instead that it is 'sufficiently smooth' for our purposes.

The linearized residual operator $R'_{jk}[\epsilon_s]$ is defined by

$$R'_{jk}[\epsilon_s] : F \longrightarrow Z_j \quad , \quad R'_{jk}[\epsilon_s]\delta\epsilon_s = M_j v_{jk} \quad (38)$$

where v_{jk} solves the linearized equation

$$\Delta v_{jk} + [a_k(\epsilon_b + \epsilon_s)(x) + ib\sigma(x)] v_{jk} = -a_k \delta\epsilon_s(x) u_{jk}(x) \quad (39)$$

with u_{jk} a solution of (31). This representation can be derived by perturbing

$$\epsilon_s \rightarrow \epsilon_s + \delta\epsilon_s \quad , \quad u_{jk} \rightarrow u_{jk} + v_{jk}, \quad (40)$$

plugging this into (31) and neglecting terms which are of higher than linear order in the perturbations $\delta\epsilon_s, v_{jk}$.

Notice that the right hand side of (39) can be interpreted as a 'scattering source'. We will use this concept later for solving our inverse scattering problem approximately in order to find a starting guess for the shape reconstruction scheme. But we want to mention here already that the linearization assumption built into (38), (39), namely that v_{jk} is small compared to u_{jk} , will not be necessary when solving the inverse scattering problem. That will allow us to circumvent some difficulties which often arise in high contrast inverse problems due to the occurrence of strong nonlinearities.

As our third linearized operator, we introduce the linearized forward operator $T'_{jk}[\phi]$ by putting

$$T'_{jk}[\phi] : \Phi \longrightarrow Z_j \quad , \quad T'_{jk}[\phi]\delta\phi = R'_{jk}[\Lambda(\phi)] \Lambda'[\phi]\delta\phi. \quad (41)$$

All three operators $\Lambda'[\phi]$, $R'_{jk}[\epsilon_s]$, and $T'_{jk}[\phi]$ are linear.

4.4 A nonlinear Kaczmarz-type approach

The algorithm works in a 'single-step fashion' as follows. Instead of using the data (10) for all sources and all frequencies simultaneously, we only use the data for one source and frequency at a time while updating the linearized residual operator after each determination of the corresponding incremental correction $\delta\phi$. So, in each step we will look for a solution of the equation

$$T'_{jk}[\phi]\delta\phi_{jk} = -T_{jk}(\phi) \quad (42)$$

for a given source index $j = 1, \dots, p$ and a given frequency index $k = 1, \dots, K$. After correcting ϕ by

$$\phi \longrightarrow \phi + \delta\phi_{jk}, \quad (43)$$

we use the updated residual equation (42) to compute the next correction $\delta\phi_{j'k'}$. Doing this for one equation after the other, until each of the sources q_j and each of the frequencies f_k has been considered exactly once, will yield one complete sweep of the algorithm. This procedure is similar to the Kaczmarz method for solving linear systems, or the algebraic reconstruction technique (ART) in x-ray tomography [32] and the simultaneous iterative reconstruction technique (SIRT) as presented in [16]. Related approaches have also been employed in ultrasound tomography by Natterer and Wübbeling [33], in more general bilinear inverse problems by Natterer [34], in optical tomography by Dorn [17], and in 3D-electromagnetic induction tomography (EMIT) by Dorn *et alii* [18].

4.5 The minimization problem

Let us assume now that we are given a level set function $\phi^{(n)}(x)$ and a scattering potential $\epsilon_s^{(n)}(x)$ such that $(\Omega^{(n)}, \epsilon_b + \epsilon_s^{(n)}, \phi^{(n)})$ forms an admissible triple in the sense of definition 3.3. Using a data set \tilde{G}_{jk} corresponding to the fixed source position q_j and the frequency f_k , we want to find an update $\delta\phi^{(n)}$ to $\phi^{(n)}$ such that for the admissible triple

$$\begin{aligned} & \left(\Omega^{(n+1)}, \epsilon_b + \epsilon_s^{(n+1)}, \phi^{(n+1)} \right) := \\ & \left(\Omega[\phi^{(n)} + \delta\phi^{(n)}], \epsilon_b + \Lambda(\phi^{(n)} + \delta\phi^{(n)}), \phi^{(n)} + \delta\phi^{(n)} \right) \end{aligned} \quad (44)$$

the residuals in the data corresponding to this source and this frequency vanish

$$T_{jk}(\phi^{(n+1)}) = T_{jk}(\phi^{(n)} + \delta\phi^{(n)}) = 0. \quad (45)$$

Applying a Newton-type approach, we get from (45) a correction $\delta\phi^{(n)}$ for $\phi^{(n)}$ by solving

$$T'_{jk}[\phi^{(n)}]\delta\phi^{(n)} = -T_{jk}(\phi^{(n)}) = -\left(M_j u_{jk} - \tilde{G}_{jk}\right) \quad (46)$$

where u_{jk} satisfies (31) with $\epsilon_s = \Lambda(\phi^{(n)})$

$$\Delta u_{jk} + \left[a_k(\epsilon_b + \Lambda(\phi^{(n)}))(x) + ib\sigma(x) \right] u_{jk} = q_j(x) \quad (47)$$

and

$$\epsilon_b(x) + \Lambda(\phi^{(n)})(x) = \begin{cases} \hat{\epsilon} & , \quad x \in \Omega[\phi^{(n)}] \\ \epsilon_b(x) & , \quad x \in \mathbb{R}^2 \setminus \Omega[\phi^{(n)}]. \end{cases} \quad (48)$$

Since we have only few data given for one source and one frequency, equation (46) usually will have many solutions (in the absence of noise), such that we have to pick

one according to some criterion. We choose to take that solution which minimizes the energy norm of $\delta\phi^{(n)}$

$$\text{Min } \|\delta\phi^{(n)}\|_2 \quad \text{subject to} \quad T'_{jk}(\phi^{(n)})\delta\phi^{(n)} = -\left(M_j u_{jk} - \tilde{G}_{jk}\right). \quad (49)$$

This solution can be formulated explicitly. It is

$$\delta\phi_{\text{MN}}^{(n)} = -T'_{jk}[\phi^{(n)}]^* \left(T'_{jk}[\phi^{(n)}]T'_{jk}[\phi^{(n)}]^*\right)^{-1} \left(M_j u_{jk} - \tilde{G}_{jk}\right), \quad (50)$$

where $T'_{jk}[\phi^{(n)}]^*$ denotes the adjoint operator to $T'_{jk}[\phi^{(n)}]$.

4.6 The adjoint linearized operators

In order to calculate the minimal norm solution (50), we will need practically useful expressions for the adjoints of the linearized operators of section (4.3). We will present such expressions in this section. The calculation of the actions of these operators will typically require to solve an adjoint Helmholtz problem. This explains the name 'adjoint field method' of the inversion method employed here.

To start with, a simple calculation gives us the following theorem.

Theorem 4.1 *The adjoint operator $\Lambda'[\phi]^*$ which corresponds to the linearized operator $\Lambda'[\phi]$ is given by*

$$\Lambda'[\phi]^* : F \longrightarrow \Phi \quad , \quad (\Lambda'[\phi]^* \delta\epsilon_s)(x) = -[\hat{\epsilon} - \epsilon_b(x)] \frac{\delta\epsilon_s(x)}{|\nabla\phi(x)|} C_\rho(\Gamma) \chi_{B_\rho(\Gamma)}(x). \quad (51)$$

The next theorem describes the adjoint operator $R'_{jk}[\epsilon_s]^*$ which corresponds to $R'_{jk}[\epsilon_s]$. Its proof is analogous to the proof of Theorem 4.1 in the appendix, or to the proof given in a similar situation in Dorn *et al.* [18], and is therefore omitted here.

Theorem 4.2 *Let $\zeta = (\zeta_1, \dots, \zeta_{D_j})^T \in Z_j$ and let x_{jd} , $d = 1, \dots, D_j$ be the detector positions corresponding to q_j . Then the action of the adjoint operator $R'_{jk}[\epsilon_s]^*$ on ζ is given by*

$$R'_{jk}[\epsilon_s]^* \zeta = -\frac{1}{a_k} \mathcal{R}e(\overline{u_{jk} z_{jk}}) \chi_{B_r(0)} \quad (52)$$

where u_{jk} solves

$$\Delta u_{jk} + \kappa_k(x) u_{jk} = q_j(x), \quad (53)$$

and z_{jk} solves the 'adjoint equation'

$$\Delta z_{jk} + \kappa_k(x) z_{jk} = \sum_{d=1}^{D_j} \bar{\zeta}_d \delta(x - x_{jd}) \quad (54)$$

with

$$\kappa_k(x) = a_k[\epsilon_b(x) + \epsilon_s(x)] + ib_k \sigma(x) \quad (55)$$

and a_k, b_k defined as in (7).

Finally, by combining theorems 4.1 and 4.2, we get an expression for the adjoint operator $T'_{jk}[\phi]^*$ which corresponds to the linearized forward operator $T'_{jk}[\phi]$. It is described in the following theorem.

Theorem 4.3 *Let $\zeta = (\zeta_1, \dots, \zeta_{D_j})^T \in Z_j$ and let x_{jd} , $d = 1, \dots, D_j$ be the detector positions corresponding to q_j . Then the adjoint operator $T'_{jk}[\epsilon_s]^*$ acts on ζ in the following way*

$$\begin{aligned} T'_{jk}[\phi]^* \zeta &= \Lambda'[\phi]^* R'_{jk}[\Lambda(\phi)]^* \zeta \\ &= \frac{[\hat{\epsilon} - \epsilon_b(x)]}{a_k |\nabla \phi(x)|} \mathcal{R}e(\overline{u_{jk} z_{jk}}) C_\rho(\Gamma) \chi_{B_\rho(\Gamma)}(x), \end{aligned} \quad (56)$$

where u_{jk} solves (53) and z_{jk} solves (54) with ϵ_s replaced by $\Lambda(\phi)$.

4.7 The operators $T'_{jk} T'^*_{jk}$

Let us consider the operator

$$C_{jk}^{(n)} := T'_{jk}[\phi^{(n)}] T'^*_{jk}[\phi^{(n)}] \quad (57)$$

in (50) more closely. Using (41) it gets the form

$$C_{jk}^{(n)} = R'_{jk}[\Lambda(\phi^{(n)})] \Lambda'[\phi^{(n)}] \Lambda'[\phi^{(n)}]^* R'_{jk}[\Lambda(\phi^{(n)})]^*. \quad (58)$$

With (37), (51) we see that, due to the operator $\Lambda'[\phi^{(n)}] \Lambda'[\phi^{(n)}]^*$ in (58), $C_{jk}^{(n)}$ maps first from the data space to functions in F or Φ which are supported on $B_\rho(\Gamma)$, and then back to the data space. In a discretized setting, it might happen that for a coarse mesh (and a small ρ) the number of pixels representing $B_\rho(\Gamma)$ becomes close to (or even smaller than) the number of data points. This observation lets us expect that the inversion of $C_{jk}^{(n)}$ in (50) will be highly ill-conditioned and unstable. This is confirmed by our numerical experiments so far.

Therefore, we will regularize the inversion of $C_{jk}^{(n)}$ and the action of its inverse on the right hand side of (46).

4.8 Regularization of $T'_{jk} T'^*_{jk}$

A standard way of regularization is the Tychonov-Phillips regularization scheme which amounts to replacing the operator $T'_{jk}[\phi^{(n)}] T'^*_{jk}[\phi^{(n)}]$ in (50) by the operator

$$T'_{jk}[\phi^{(n)}] T'^*_{jk}[\phi^{(n)}] + \lambda I \quad (59)$$

with some suitably chosen regularization parameter $\lambda > 0$. A small λ means little regularization, whereas in the case of very noisy data we might wish to use a very

large λ such that (59) is dominated by the term λI and we can approximate it further by a simple multiplication with the regularization parameter λ .

However, motivated by the above mentioned observations, we choose a different form of regularization. First, we add a Tychonov-Phillips term to $\Lambda'[\phi^{(n)}] \Lambda'[\phi^{(n)}]^*$ such that the right hand side of (58) becomes

$$C_{jk}^{(n)} \approx R'_{jk}[\Lambda(\phi^{(n)})] \left(\Lambda'[\phi^{(n)}] \Lambda'[\phi^{(n)}]^* + \lambda I \right) R'_{jk}[\Lambda(\phi^{(n)})]^*. \quad (60)$$

Now, using a very large regularization parameter λ , we approximate (60) further by

$$C_{jk}^{(n)} \approx \lambda R'_{jk}[\Lambda(\phi^{(n)})] R'_{jk}[\Lambda(\phi^{(n)})]^*. \quad (61)$$

Since calculating the operator (61) in each step of the inversion routine is still very time-consuming, we approximate this operator further by replacing the argument $\Lambda(\phi^{(n)})$ by the background scattering potential which is zero. Therefore, we end up with the following approximation for $C_{jk}^{(n)}$

$$C_{jk}^{(n)} \approx \hat{C}_{jk} := R'_{jk}[0] R'_{jk}[0]^* \quad \text{for all } n = 1, 2, \dots \quad (62)$$

The multiplier λ is neglected in (62) since it becomes part of the relaxation parameter in our inversion scheme. We see that we have replaced in (62) the highly ill-conditioned and difficult to calculate operator $C_{jk}^{(n)}$ by a much better conditioned operator \hat{C}_{jk} which has to be computed only once and which can be precalculated before starting the inversion routine.

The next theorem tells us how to practically compute the operator \hat{C}_{jk} for a given background permittivity ϵ_b .

Theorem 4.4 *Let us assume that we are given a background permittivity distribution ϵ_b , a finite set of sources q_j , $j = 1, \dots, p$, and for each of these sources a finite set of receiver positions x_{jd} , $d = 1, \dots, D_j$. We apply each of the sources with K different frequencies f_k , $k = 1, \dots, K$. The operators \hat{C}_{jk} , $j = 1, \dots, p$, $k = 1, \dots, K$, are then described by $D_j \times D_j$ matrices of the form*

$$\hat{C}_{jk} = \left\{ \int_{B_r(0)} \overline{u_{jk}(x) \varphi_{dk}(x)} u_{jk}(x) \varphi_{lk}(x) \right\}_{\substack{l=1, \dots, D_j \\ d=1, \dots, D_j}}, \quad (63)$$

where $\varphi_{\nu k}$ solves

$$\Delta \varphi_{\nu k} + (a_k \epsilon_b + i b_k \sigma) \varphi_{\nu k} = \delta(x - x_{j\nu}) \quad (64)$$

and u_{jk} solves

$$\Delta u_{jk} + (a_k \epsilon_b + i b_k \sigma) u_{jk} = q_j. \quad (65)$$

The index ν in (64) can stand for a receiver index d or l . In (63), the receiver index l is the row index, and the receiver index d is the column index of \hat{C}_{jk} .

The proof of this theorem is similar to the proof of Theorem 5.2 given in the appendix such that we omit it here.

4.9 Updating the level set function

In order to calculate a correction $\delta\phi_{\text{MN}}^{(n)}$ by (50) we have to apply the operator $T'_{jk}[\phi^{(n)}]^*$ to the vector

$$\zeta := \hat{C}_{jk}^{-1} \left(M_j u_{jk} - \tilde{G}_{jk} \right). \quad (66)$$

An explicit formula for $T'_{jk}[\phi^{(n)}]$ was already given in (56)

$$T'_{jk}[\phi^{(n)}]^* \zeta = \frac{[\hat{\epsilon} - \epsilon_b(x)]}{a_k |\nabla \phi^{(n)}(x)|} \mathcal{R}e \left(\overline{u_{jk}(x) z_{jk}(x)} \right) C_\rho(\Gamma) \chi_{B_\rho(\Gamma)}(x), \quad (67)$$

where u_{jk} and z_{jk} solve (53)- (55) with ϵ_s replaced by $\Lambda(\phi^{(n)})$.

To stabilize the reconstruction scheme, we replace the term $|\nabla \phi(x)|$ in (67) by some constant c_1 . Doing so we avoid dividing by numerical derivatives which might cause instabilities due to numerical noise and roundoff errors. This is justified as long as $|\nabla \phi(x)|$ does not vary too much along the boundary. It turns out that the updates we apply in our numerical examples to the level set functions usually justify this assumption. In cases with limited view and very noisy data, however, we will apply an additional 'smoothing procedure' (which is described in section 4.10) to the level set functions near the boundary after each update in order to guarantee the necessary regularity for the succeeding steps.

With these modifications, (50) yields the following *update formula for the level set function*

$$\delta\hat{\phi}^{(n)}(x) = - \frac{\hat{\epsilon} - \epsilon_b(x)}{c_1 a_k} \mathcal{R}e \left(\overline{u_{jk}(x) z_{jk}(x)} \right) C_\rho(\Gamma) \chi_{B_\rho(\Gamma)}(x) \quad (68)$$

where u_{jk} and z_{jk} solve (53)- (55) with ζ given by (66) and ϵ_s replaced by $\Lambda(\phi^{(n)})$.

Notice that, although we did not explicitly impose any regularity constraints on the updates (68), they are in the range of $R'_{jk}[\Lambda(\phi^{(n)})]^*$ (up to the factor $\hat{\epsilon} - \epsilon_b(x)$) which implicitly gives us some information about the regularity we can expect. Our numerical experiments so far indicate that the degree of regularity which is achieved by applying (68) is typically sufficient 'for practical purposes' in those situations where the data are not too noisy and where we have suitably arranged receiver positions all around the obstacles. (This is the 'full view' situation.)

However, in cases of noisy and limited-view data, the resulting boundaries look rough and fuzzy, in particular when high-frequency data are used for the reconstruction. In these situations, we can improve the results by applying some additional regularization on ϕ . A possible way of doing so is to filter the level set function after

each update in order to smooth it locally. An example for such a procedure is 'curve shortening by diffusion', which is briefly described at the end of section 4.10.

We mention that an interesting (and from a mathematical point of view more satisfactory) alternative to this procedure would be to apply some additional regularity constraints already in the derivation of (68), such that we would not have to worry at all about the smoothness of the resulting level set functions. We will investigate possible ways of doing so in our future research.

4.10 Implementation: The levelART algorithm

In brief algorithmic form, the nonlinear Kaczmarz-type method for shape reconstruction using level sets (which we call for short 'levelART' because of its above mentioned similarity to the 'ART' algorithm in x-ray tomography) can be written in the following way.

Preparation step.

- Calculate \hat{C}_{jk} and

$$D_{jk} = \hat{C}_{jk}^{-1} \quad (69)$$

according to (63) for each source q_j , $j = 1, \dots, p$, and each frequency f_k , $k = 1, \dots, K$, and store in memory for later use.

- Build groups of frequencies $G_m = \{f_1, \dots, f_{K_m}\}$, $m = 1, \dots, M$.

Initialization.

$n = 0$;

$(\Omega^{(0)}, \epsilon^{(0)}, \phi^{(0)})$ given from STAF.

Reconstruction loop.

```

FOR  $m = 1 : M$       march over frequency groups  $G_m$ 
  FOR  $i = 1 : I_m$     perform  $I_m$  sweeps for frequency group  $G_m$ 
    FOR  $k = 1 : K_m$   march over frequencies in  $G_m$ 
      FOR  $j = 1 : p$    march over sources  $q_j$  for each frequency
         $\zeta_{jk} = D_{jk}(M_j u_{jk} - \tilde{G}_{jk})$ ;     $u_{jk}$  solves (53) with  $\epsilon^{(n)}$ 
         $\delta\phi_{jk} = -\frac{\hat{\epsilon} - \epsilon_b(x)}{a_k} \mathcal{R}e(\overline{u_{jk} z_{jk}}) \chi_{B_\rho(\Gamma)}$ ;   $z_{jk}$  solves (54) with  $\epsilon^{(n)}$  and  $\zeta_{jk}$ 
      END
       $\delta\phi^{(n)}(x) = \sum_{j=1}^p \delta\phi_{jk}(x)$ ;
       $\phi^{(n+1)} = C_{\text{LS}}^{(n)}(\phi^{(n)} + \eta \frac{C_\rho(\Gamma)}{c_1} \delta\phi^{(n)})$ ;      update level set function
      Optional step: 'curve shortening' by diffusion. See separate chart.
       $\epsilon^{(n+1)} = \epsilon_b + \Lambda(\phi^{(n+1)})$ ;   $n = n + 1$ ;      Reinitialization  $n \rightarrow n + 1$ 
    END
  END
  alternatively, some stopping criteria can be used here
END
END
 $(\Omega^{(N)}, \epsilon^{(N)}, \phi^{(N)}) = (\Omega[\phi^{(n)}], \epsilon_b + \Lambda(\phi^{(n)}), \phi^{(n)})$ ;      Final reconstruction.

```

Here, η is a relaxation parameter for the update of the level set function which is determined empirically. The constant $C_\rho(\Gamma)$ could be calculated explicitly for the actual curve $\Gamma^{(n)}$, or it could be approximated by some value corresponding to a simple geometrical object (to give an example, in case of a single circle it would be $C_\rho(\Gamma) = (2\rho)^{-1}$). In our numerical experiments so far, however, it is simply considered as part of η . The same holds true for c_1 . The constant ρ is in our numerical experiments chosen between 30-40 cm, which corresponds to 2-3 grid cells. The scaling factor $C_{\text{LS}}^{(n)}$ is determined after each update to keep the global minimum (or maximum) of the level set function at a constant value.

The following smoothing filter on the level set function is optional. We usually apply it when we use noisy high-frequency data for the reconstruction. Especially in the limited-view examples presented in sections 6.3 and 6.4, the application of this filter improves the reconstructions significantly. Smoothing the level set function with this filter has the effect of local curve shortening. Roughness and small scale oscillations in the reconstructed boundaries are smoothed out such that the 'energy' of the reconstructed boundaries is reduced. The filtering step can be described as follows.

Optional step: 'Curve shortening' by diffusion.

Introduce artificial time $\tau \in \mathbb{R}$. $\frac{\partial}{\partial \tau}$ = time derivative, Δ = Laplace operator.

Solve initial value problem (with absorbing boundary conditions) on $B_r(0)$:

$$\begin{aligned}\tilde{\phi}(x, 0) &= \phi^{(n+1)}(x); \\ \frac{\partial}{\partial \tau} \tilde{\phi}(x, \tau) &= \Delta \tilde{\phi}(x, \tau), \quad \tau \in [0, T_\lambda], \quad x \in B_r(0). \\ \phi^{(n+1)}(x) &= \tilde{\phi}(x, T_\lambda),\end{aligned}$$

with regularization parameter T_λ .

5 Step 1: A Source-Type Adjoint Field method

For starting our shape reconstruction method using level sets we will need an initial guess $(\Omega^{(0)}, \epsilon^{(0)}, \phi^{(0)})$.

Although it is possible just to create an arbitrary initial guess without using any data at all, we believe that it is important for the efficiency and the robustness of such a method to start it with a *good* initial guess. There are several reasons for this. First, when deriving the shape reconstruction method (which we will call for short 'levelART' in the following) we used a perturbation approach which is strictly

justified only when we already have a good first guess available. Moreover, we see in our numerical experiments that starting with a good initial guess stabilizes the shape reconstruction routine, in particular in cases where the data are incomplete and noisy. In addition, finding a good first guess reduces the amount of work which has to be done by the levelART routine itself, such that in the end the combined code will converge much more rapidly than levelART alone would do without a good initialization.

In this section, we will present the second key point of our combined inversion scheme, namely a *fast*, *inexpensive* and *stable* method for finding a very good first guess $(\Omega^{(0)}, \epsilon^{(0)}, \phi^{(0)})$ for levelART. This method is designed to share basic features with the levelART algorithm, such that it can be implemented in addition to levelART with almost no extra cost.

5.1 Source-type methods

In the framework of inverse scattering problems, the method we propose here can be considered as a 'source-type inversion method'. Roughly speaking, the general idea of source-type reconstruction methods in inverse scattering is to split a given nonlinear inverse scattering problem into two subproblems. The first one is linear, and tries to recover a virtual 'equivalent source' in the medium which would be able to fit the data if applied with the known background distribution. This equivalent source is related to the unknown scattering potential by a nonlinear 'constitutive' relation. Therefore, in the second part of the algorithm, a nonlinear inverse problem has to be solved to derive the scattering potential from the recovered equivalent source distribution.

This idea is not at all new. It has been applied for example in the Source-Type Integral Equation (STIE) method of Habashy *et al* [21], or in the method presented by Chew *et al.* in [9]. More recently, similar ideas have been applied by Abdullah *et al.* [1], Caorsi *et al.* [6], and van den Berg *et al.* [46, 47].

All of these approaches have in common that they use the source-type method as a stand-alone inversion scheme. Such a method has the advantage that it is not as sensitive to strong nonlinearities in the inverse problem as for example perturbation methods or the Born or Rytov approximation are [15, 20, 27].

On the other hand, interpreting the inverse scattering problem as an inverse source problem is not without drawbacks. For example, the existence of so-called 'non-radiating sources' or 'invisible sources' gives rise to a nonuniqueness in the inverse source problem, which is difficult to deal with when solving the nonlinear part [1, 14, 21]. Moreover, it is not clear at all how to combine properly the information corresponding to different experiments, since each experiment creates its own 'equiv-

alent sources' and its own 'invisible sources'. For more information about possible applications, advantages and drawbacks of the source-type scheme as a stand-alone inversion tool we refer to [1, 5, 6, 9, 14, 21, 46, 47].

Our approach is different from those mentioned above. We only want to find a good *approximation* to the scattering potential, and a corresponding *initial level set function* suitable to start the shape reconstruction routine. Moreover, we can make use of our prior information about the permittivity distribution. This will allow us to circumvent most of the problems of source-type schemes which have been mentioned above.

We will now describe this method, which we will call the Source-Type Adjoint Field (STAF) method, in more details.

5.2 Solving the inverse scattering problem

Consider the inverse scattering problem formulated in section 3.1. The decomposition (13), (14) reads

$$\tilde{\epsilon}(x) = \epsilon_b(x) + \tilde{\epsilon}_s(x) \quad (70)$$

with some (known) background distribution ϵ_b and the (unknown) scattering potential $\tilde{\epsilon}_s$ having compact support, $\text{supp}(\tilde{\epsilon}_s) \subset \subset B_r(0)$. The goal is to find $\tilde{\epsilon}_s(x)$ from the data (9).

We already mentioned above that we actually will *not* recover the entire function $\tilde{\epsilon}_s(x)$ from the data \tilde{G}_{jk} in this preprocessing step. All we will find is 1.) A very good first guess for the scattering potential $\epsilon_s^{(0)}$ which will be part of the initializing triple $(\Omega^{(0)}, \epsilon_b + \epsilon_s^{(0)}, \phi^{(0)})$, and 2.) A corresponding level set function $\phi^{(0)}$. We will freely make use of the prior information resulting from the knowledge of $\hat{\epsilon}$ inside the estimated scatterer $\Omega^{(0)}$. However, our numerical results so far indicate that the method proposed here -if suitably adapted- can actually be used to find, in addition to $\Omega^{(0)}$ and $\phi^{(0)}$, also a good first estimate $\hat{\epsilon}^{(0)}$ for the contrast $\hat{\epsilon}$. This will be used in our future work to start a reconstruction method which tries to recover $\tilde{\Omega}$ and $\hat{\epsilon}$ *simultaneously* from the given data.

For a fixed frequency f_k and a source q_j , let \tilde{u}_{jk} be the solution of

$$\Delta \tilde{u}_{jk} + (a_k(\epsilon_b + \tilde{\epsilon}_s)(x) + ib\sigma(x)) \tilde{u}_{jk} = q_j(x), \quad (71)$$

and let u_{jk} be the solution of the 'unperturbed' equation

$$\Delta u_{jk} + (a_k \epsilon_b(x) + ib\sigma(x)) u_{jk} = q_j(x). \quad (72)$$

Define

$$\tilde{v}_{jk} := u_{jk} - \tilde{u}_{jk}. \quad (73)$$

Subtraction of (72) from (71) shows that \tilde{v}_{jk} solves

$$\Delta \tilde{v}_{jk} + (a_k \epsilon_b(x) + ib\sigma(x)) \tilde{v}_{jk} = \tilde{Q}_{jk}^s(x), \quad (74)$$

where the 'scattering source' $\tilde{Q}_{jk}^s(x)$ is defined as

$$\tilde{Q}_{jk}^s(x) = a_k \tilde{\epsilon}_s(x) \tilde{u}_{jk}(x). \quad (75)$$

We introduce a 'source type' forward operator A_{jk} by putting

$$A_{jk} : Y \longrightarrow Z_j \quad , \quad A_{jk} Q_{jk}^s = M_j v_{jk} \quad (76)$$

where M_j is the measurement operator defined in (8), and v_{jk} solves

$$\Delta v_{jk} + (a_k \epsilon_b(x) + ib\sigma(x)) v_{jk} = Q_{jk}^s(x). \quad (77)$$

The operator A_{jk} is linear.

Let us assume now that we apply the 'correct' scattering source $\tilde{Q}_{jk}^s(x)$ defined by (75) as argument of A_{jk} . Then we know from (9), (29), (30) that

$$A_{jk} \tilde{Q}_{jk} = M_j \tilde{v}_{jk} = M_j (u_{jk} - \tilde{u}_{jk}) = M_j u_{jk} - \tilde{G}_{jk} = R_{jk}(0). \quad (78)$$

The vectors $R_{jk}(0)$ are easily computed by solving a forward problem on the background distribution (72). Therefore, all we have to do to get back the scattering source \tilde{Q}_{jk}^s from the data \tilde{G}_{jk} is to solve (78) for \tilde{Q}_{jk}^s . Doing so amounts to solving an ill-posed but *linear* inverse problem.

Once we have recovered $\tilde{Q}_{jk}^s(x)$, we want to get back $\tilde{\epsilon}_s(x)$ out of it by using the constitutive relation (75). This second part of the inversion scheme can be interpreted as solving a *nonlinear* inverse problem since $\tilde{u}_{jk}(x)$ depends on $\tilde{\epsilon}_s(x)$.

Notice that $\tilde{Q}_{jk}^s(x)$ varies with different sources and frequencies, but that $\tilde{\epsilon}_s(x)$ is the same for all sources and all frequencies (if we neglect dispersion). We will make use of this observation when we try to solve the nonlinear part (75). In the following, we describe the method which we will use to recover the scattering source $\tilde{Q}_{jk}^s(x)$ from a given data set \tilde{G}_{jk} for a fixed source q_j and a fixed frequency f_k .

5.3 Looking for a scattering source

Since for a fixed (primary) source position and a fixed frequency we have only few data given to recover \tilde{Q}_{jk}^s , and since we have to take into account that also 'non-radiating' and 'invisible' sources have been generated in the experiment, we assume that there will be many solutions (in absence of noise) of (78). To pick one we are looking for the solution with minimal norm

$$\text{Min } \|Q_{jk}^s\|_Y \quad \text{subject to} \quad A_{jk} Q_{jk}^s = R_{jk}(0). \quad (79)$$

It is given by

$$Q_{jk,MN}^s = A_{jk}^* \left(A_{jk} A_{jk}^* \right)^{-1} R_{jk}(0), \quad (80)$$

where A_{jk}^* denotes the adjoint operator to A_{jk} .

The following theorem, which is proven in the appendix, tells us how to calculate the action of A_{jk}^* on a vector $\zeta \in Z_j$ in an efficient way.

Theorem 5.1 *Let $\zeta = (\zeta_1, \dots, \zeta_{D_j})^T \in Z_j$ and let x_{jd} , $d = 1, \dots, D_j$ be the detector positions corresponding to the source q_j . Then, $A_{jk}^* \zeta$ is given by*

$$A_{jk}^* \zeta = \overline{z_{jk}} \chi_{B_r(0)}, \quad (81)$$

where z_{jk} solves

$$\Delta z_{jk} + (a_k \epsilon_b + i b_k \sigma) z_{jk} = \sum_{d=1}^{D_j} \overline{\zeta_d} \delta(x - x_{jd}). \quad (82)$$

Corollary 5.1 *Let $\varphi_{\nu k}$ solve*

$$\Delta \varphi_{\nu k} + (a_k \epsilon_b + i b_k \sigma) \varphi_{\nu k} = \delta(x - x_{j\nu}). \quad (83)$$

Then, we can write (81) in the alternative form

$$\left(A_{jk}^* \zeta \right) (x) = \overline{\sum_{d=1}^{D_j} \zeta_d \varphi_{dk}(x) \chi_{B_r(0)}(x)} = \sum_{d=1}^{D_j} \zeta_d \overline{\varphi_{dk}(x) \chi_{B_r(0)}(x)}. \quad (84)$$

The next theorem, which is proven in the appendix, gives an explicit expression for the operators $A_{jk} A_{jk}^*$.

Theorem 5.2 *Let us assume that we are given a background permittivity distribution ϵ_b and a finite set of receiver positions x_{jd} , $d = 1, \dots, D_j$. The operators $A_{jk} A_{jk}^*$, $j = 1, \dots, p$, $k = 1, \dots, K$, are then described by $D_j \times D_j$ matrices of the form*

$$A_{jk} A_{jk}^* = \left\{ \int_{B_r(0)} \overline{\varphi_{dk}(x)} \varphi_{lk}(x) \right\}_{\substack{l=1, \dots, D_j \\ d=1, \dots, D_j}}, \quad (85)$$

where $\varphi_{\nu k}$ solves (83) and the index ν can stand for a receiver index d or l . In (85), the receiver index l is the row index, and the receiver index d is the column index of \hat{C}_{jk} .

Remark. Notice that (85) does not depend on the sources q_j , but only on the arrangement of the detectors and on the background permittivity distribution ϵ_b . The operators $A_{jk} A_{jk}^*$ can be precomputed before starting the inversion routine,

and this has to be done only once for each frequency as long as we use the same arrangement of detectors for all sources q_j , $j = 1, \dots, p$.

In the case of noisy data we will invert $A_{jk}A_{jk}^* + \lambda I$ instead of $A_{jk}A_{jk}^*$ in (80) with a suitably chosen regularization parameter $\lambda > 0$. This amounts to applying Tychonov-Phillips regularization.

5.4 Recovery of the scattering potential

After we have found a scattering source Q_{jk}^s which satisfies (79), we want to use the constitutive relation

$$Q_{jk}^s(x) = a_k \tilde{\epsilon}_s(x) \tilde{u}_{jk}(x), \quad (86)$$

which holds for the 'correct' scattering source \tilde{Q}_{jk}^s according to (75), to find an approximation for $\tilde{\epsilon}_s(x)$.

Let \tilde{u}_{jk} be a solution of (71) and u_{jk} a solution of (72). We decompose Q_{jk}^s , \tilde{u}_{jk} , u_{jk} and $\tilde{\epsilon}_s$ into amplitude and phase

$$Q_{jk}^s(x) = |Q_{jk}^s(x)| e^{ir(x)}, \quad \tilde{u}_{jk} = |\tilde{u}_{jk}| e^{i\tilde{s}(x)}, \quad (87)$$

$$u_{jk} = |u_{jk}| e^{is(x)}, \quad \epsilon_s(x) = |\epsilon_s(x)| e^{it(x)}, \quad (88)$$

where we have omitted the subscripts jk in the argument functions r , \tilde{s} , s , and t for simplicity in the notation. Making use of the fact that $\tilde{\epsilon}_s(x) \in \mathbb{R}$ we see that

$$t(x) \in \{0, \pi\} \quad \text{for all } x \in \mathbb{R}^2. \quad (89)$$

With (87),(88) equation (79) decomposes into two equations, one for the amplitude and one for the phase. They are

$$|Q_{jk}^s(x)| = a_k |\tilde{\epsilon}_s(x)| |\tilde{u}_{jk}|, \quad (90)$$

$$r(x) = \tilde{s}(x) + t(x). \quad (91)$$

The observation in our numerical experiments is that, although $s(x)$ and $\tilde{s}(x)$ might be quite different from each other for large perturbations $\tilde{\epsilon}_s(x)$, the amplitudes $|u_{jk}(x)|$ and $|\tilde{u}_{jk}(x)|$ most often do not differ too much from each other in the scattering region. Therefore, in our applications it is a reasonable approximation to assume that

$$|\tilde{u}_{jk}(x)| \approx |u_{jk}(x)| \quad \text{in } B_r(0). \quad (92)$$

With this approximation, (90) yields the following estimate for $|\tilde{\epsilon}_s(x)|$

$$|\tilde{\epsilon}_s^{(jk)}(x)| \approx \frac{|Q_{jk}^s(x)|}{a_k |u_{jk}(x)|} \quad \text{in } B_r(0). \quad (93)$$

We have added the indices j and k on the left hand side of (93) to indicate that we have used only the data \tilde{G}_{jk} corresponding to source q_j and frequency f_k for its determination.

Notice that the step (92), (93) is *nonlinear* since taking the amplitude of a complex number is a nonlinear operation. Therefore, the approach presented here is quite different from the usual Born approximation which approximates \tilde{u}_{jk} by u_{jk} .

For the purposes of the present paper, the determination of $|\tilde{\epsilon}_s(x)|$ is already sufficient in order to get a good first guess for the scattering potential $\epsilon_s^{(0)}(x)$ and for the level set function $\phi^{(0)}(x)$, since we can now make use of our prior information about the correct value of $\hat{\epsilon}$ in (12).

We mention, however, that the recovery of the phase $t(x)$ is also possible from (86). (This will be necessary for example when we try to recover $\tilde{\Omega}$ and $\hat{\epsilon}$ simultaneously from the given set of data \tilde{G}_{jk} .) We can do this by using equation (91). We already mentioned that the assumption $\tilde{s}(x) \approx s(x)$ might be quite wrong for situations with large scattering potentials $\tilde{\epsilon}_s(x)$. However, in our situation we only have to decide whether $t(x)$ is zero or π , which means that we have to determine whether in (91) $r(x) = \tilde{s}(x)$ or $r(x) = \tilde{s}(x) \pm \pi$ is satisfied. Therefore, a reasonable estimate for $t(x)$ is to put

$$t^{(jk)}(x) = \begin{cases} 0 & , \quad |s(x) - r(x)| < \pi/2, \\ \pi & , \quad \text{elsewhere.} \end{cases} \quad (94)$$

Our numerical experiments so far show that a suitable combination of these estimates resulting from many source positions gives a very good reconstruction of the phase $t(x)$ in $B_r(0)$ even in the situation of limited view and noisy data. We will not need this estimate in the present paper.

5.5 Combining the results from single experiments

We can combine now the estimates $|\tilde{\epsilon}_s^{(jk)}(x)|$ from many source positions q_j , $j = 1, \dots, p$, by putting

$$|\tilde{\epsilon}_s^{(k)}(x)| = \frac{1}{p} \sum_{j=1}^p |\tilde{\epsilon}_s^{(jk)}(x)|. \quad (95)$$

If we want to take into account also the information corresponding to many frequencies we can do so by putting

$$|\tilde{\epsilon}_s(x)| \approx \frac{1}{pK} \sum_{k=1}^K \sum_{j=1}^p |\tilde{\epsilon}_s^{(jk)}(x)| \quad (96)$$

where the sum is over all frequencies f_k , $k = 1, \dots, K$, and all source positions q_j , $j = 1, \dots, p$. In (96) we have neglected dispersion.

A similar strategy can be employed to improve the estimates for the phase $t^{(jk)}(x)$.

5.6 The initial level set function

We are now ready to define the initial triple $(\Omega^{(0)}, \epsilon^{(0)}, \phi^{(0)})$.

We assume that we are working in a high contrast situation, such that exactly one of the following conditions is satisfied

$$\hat{\epsilon} - \epsilon_b(x) \gg 0 \quad \text{for all } x \in \tilde{\Omega} \quad (97)$$

$$\hat{\epsilon} - \epsilon_b(x) \ll 0 \quad \text{for all } x \in \tilde{\Omega}. \quad (98)$$

Since we know $\hat{\epsilon}$ and $\epsilon_b(x)$, we know the constant

$$\text{sign}(\tilde{\Omega}) := \begin{cases} 1 & , \quad \text{if (97) holds} \\ -1 & , \quad \text{if (98) holds.} \end{cases} \quad (99)$$

Let us assume that we want to use $|\tilde{\epsilon}_s^{(k)}(x)|$ as defined in (95) for a fixed frequency f_k to specify the level set function $\phi^{(0)}$. Choose a threshold value $0 < \gamma_{\text{LS}} < 1$ (in our numerical examples presented in section 6 we use $\gamma_{\text{LS}} = 0.7$) and define

$$\epsilon_{\text{LS}} := \gamma_{\text{LS}} \max_{x \in B_r(0)} |\tilde{\epsilon}_s^{(k)}(x)|. \quad (100)$$

For the level set zero $L_0^{(0)}$ of $\phi^{(0)}$ we require that

$$L_0^{(0)} = \left\{ x \in B_r(0) : |\tilde{\epsilon}_s^{(k)}(x)| = \epsilon_{\text{LS}} \right\}. \quad (101)$$

This means that we want all points of $B_r(0)$ where the reconstruction $|\tilde{\epsilon}_s^{(k)}(x)|$ has exactly the value ϵ_{LS} to be mapped to zero by the level set function $\phi^{(0)}$

$$\phi^{(0)}(x) = 0 \quad \text{for all } x \in L_0^{(0)}. \quad (102)$$

The level set function is now defined as

$$\phi^{(0)}(x) = C_{\text{LS}}^{(0)} \text{sign}(\tilde{\Omega}) \left(\epsilon_{\text{LS}} - |\tilde{\epsilon}_s^{(k)}(x)| \right), \quad (103)$$

where $C_{\text{LS}}^{(0)}$ is some suitably chosen scaling factor. Notice that (102) and (103) are consistent.

The initial scattering domain $\Omega^{(0)}$ and the permittivity $\epsilon^{(0)}$ are defined as

$$\Omega^{(0)} = \Omega[\phi^{(0)}], \quad \epsilon^{(0)} = \epsilon_b + \Lambda(\phi^{(0)}). \quad (104)$$

Together with $\phi^{(0)}$ they form an admissible triple $(\Omega^{(0)}, \epsilon^{(0)}, \phi^{(0)})$.

5.7 Implementation: The STAF algorithm

In brief algorithmic form, the Source Type Adjoint Field (STAF) scheme can be written in the following way.

Preparation step.

- Select a group of frequencies $G_s = \{f_1, \dots, f_{K_s}\}$ which are used for the STAF reconstruction. Typically, this is just one frequency.
- Calculate $A_{jk}A_{jk}^*$ according to (85) for each frequency $f \in G_s$. The operator $A_{jk}A_{jk}^*$ does not depend on the index j if we use the same detector positions for all sources.
- Calculate

$$B_{jk} = (A_{jk}A_{jk}^*)^{-1} \quad \text{or} \quad B_{jk} = (A_{jk}A_{jk}^* + \lambda I)^{-1} \quad (105)$$

for all $f \in G_s$ and store in memory for later use.

Reconstruction step.

FOR $k = 1 : K_s$

FOR $j = 1 : p$

$$R_{jk}(0) = M_j u_{jk} - \tilde{G}_{jk}, \quad u_{jk} \text{ solves (72)}$$

$$\zeta_{jk} = B_{jk} R_{jk}(0), \quad B_{jk} \text{ from (105)}$$

$$Q_{jk}^s = A_{jk}^* \zeta_{jk} = \overline{z_{jk}} \chi_{B_r(0)}, \quad z_{jk} \text{ solves (82)}$$

$$|\tilde{\epsilon}_s^{(jk)}(x)| = \frac{|Q_{jk}^s(x)|}{a_k |u_{jk}(x)|}$$

END

END

$$|\tilde{\epsilon}_s(x)| = \frac{1}{pK_s} \sum_{k=1}^{K_s} \sum_{j=1}^p |\tilde{\epsilon}_s^{(jk)}(x)|, \quad x \in B_r(0)$$

$$\phi^{(0)}(x) = C_{\text{LS}}^{(0)} \text{sign}(\tilde{\Omega})(\epsilon_{\text{LS}} - |\tilde{\epsilon}_s(x)|) \quad \text{as in (103)}$$

$$(\Omega^{(0)}, \epsilon^{(0)}, \phi^{(0)}) = (\Omega[\phi^{(0)}], \epsilon_b + \Lambda(\phi^{(0)}), \phi^{(0)}).$$

6 Numerical Experiments

6.1 Discretization of the computational domain.

In our numerical experiments, we use a Finite-Differences Frequency Domain (FDFD) code written in MATLAB for solving (1)-(3). The code uses appropriately designed

perfectly matched layers (PML) to avoid reflections at the artificial computational boundaries [36, 37].

The system which results after discretization is solved by a simple Gauss elimination scheme, which is reflected in the implementation shown in sections 4.10 and 5.7. The LR -factorization corresponding to the most recent best guess is used there to calculate the fields for all transmitters and all receivers simultaneously. Therefore, the computational cost for solving all necessary forward and adjoint problems is just one LR -factorization for STAF, and one LR -factorization per update for levelART. If a different solver is used (e.g. GMRES or QMR), then we might find more efficient strategies than those presented in sections 4.10 and 5.7. We mention also that an iterative solver has been developed recently in [25] which is optimized to work on several source distributions simultaneously.

The physical domain is partitioned into 100×100 elementary cells (pixels) in the first numerical example, and into 180×110 elementary cells in the second and third example. Each of these grid cells has a physical size of about $0.14 \times 0.14 \text{ m}^2$, such that the total computational domain in the first example covers an area of $14 \times 14 \text{ m}^2$, and in the other two examples of $15 \times 25 \text{ m}^2$. The eight layers which are closest to the boundaries of the computational domain are used as a PML.

We will refer to the first numerical example as the 'full-view' situation, and to the other two numerical examples as the 'limited-view', 'cross-borehole' or 'geophysical' situations. This terminology is motivated by the source and receiver geometries used, which are as follows.

In the full-view example, we have 64 sources and receivers given which surround the domain of interest. Each source position is at the same time a receiver position and vice versa. The distance of two adjacent sources or receivers from each other is four pixels or about 55 cm. The area enclosed by these sources and receivers has a size of $10 \times 10 \text{ m}^2$.

In the two limited-view examples, 74 sources and receivers are positioned equally spaced in two boreholes. The distance of two adjacent sources or receivers from each other is again 4 pixels or 55 cm, and the distance of the two boreholes from each other is about 10 m.

We mention that, in all of our numerical examples, the regions beyond the source and receiver positions are part of the inversion problem, too. This means, the area which has to be recovered from the data is the whole area situated between the PML boundaries. In some of our numerical experiments, artifacts can be observed developping in the outer areas during the early stages of the reconstruction process.

We apply time-harmonic dipole sources of the form (11) with frequencies of $f = 5, 10, 15, 20, 25$, or 30 MHz . In our examples, this corresponds to wavelengths

in the background medium between 2 meters for $f = 30$ MHz and 13 meters for $f = 5$ MHz. The size of an individual grid cell is chosen such that each of these wavelengths is sampled by at least 16 pixels in order to avoid numerical artifacts due to undersampling.

The data in our numerical examples are generated by running the FDFD forward modelling code on the correct permittivity and conductivity distributions. Using the same forward code for creating the data and for doing the reconstruction is usually called 'inverse crime'. Therefore, to make sure that the situations we model in our experiments are as realistic as possible, we have tested the forward modelling code thoroughly, and add Gaussian noise with signal-to-noise ratios between 10 and 5 dB to the real and imaginary parts of the generated data.

6.2 A full-view example

Our first numerical example tests whether the derived algorithm is able to reconstruct a relatively complicated shape in the ideal situation where sources and receivers completely surround the area of interest. The geometry of this example is shown in Figure 1. The positions of the sources and receivers are indicated by dots in the Figure. The background medium in this example consists of a homogeneous conductivity distribution $\sigma_b = 3.0 \times 10^{-4}$ Siemens/m, and a homogeneous permittivity distribution $\epsilon_b = 20$. Inside the object, the permittivity is $\hat{\epsilon} = 15$, having a moderate contrast to the background distribution.

Notice that an interesting feature of this geometry is the 'hole' in the body of the object which is difficult to reconstruct. We will see that, during the evolution of the permittivity in levelART, the boundaries of the reconstructed domain will split and merge in the attempt to recover this geometry correctly.

First, we test the STAF algorithm in Figure 2 by reconstructing the permittivity $\epsilon^{(0)}$ using only the data $G_s = \{30 \text{ MHz}\}$. These data are noisy with a signal-to-noise ratio (SNR) of 10 dB in the real and the imaginary parts. Compare the result with the upper left image of Figure 3 where we used (noise-free) data with frequency $G_s = \{5 \text{ MHz}\}$.

A comparison of reconstructed permittivities for different frequencies between 5 and 30 MHz shows that -in the ideal situation of sources and receivers completely surrounding the area of interest- the STAF algorithm usually yields already a decent approximation to the shape of the inclusion when applied to the data with the highest frequencies, whereas it yields a reconstruction with decreasing resolution when applied to data corresponding to lower frequencies.

Therefore, it seems to be most efficient to apply the STAF algorithm directly to the highest frequency data, such that we do not need at all any low-frequency

information for the reconstruction. We will see in the following two geophysical examples that this is certainly not true in applications where we have only data with limited view available. In these cases, the use of lower frequency data stabilizes the reconstruction process, and is necessary for preparing the final reconstruction step using the higher frequency data.

We also want to demonstrate the performance of the levelART reconstruction scheme when applied to this geometry. We start the algorithm by using as initial permittivity $\epsilon^{(0)}$ the low resolution STAF reconstruction which is shown in the upper left image of Figure 3, and the corresponding initial level set function $\phi^{(0)}$. No noise is added to the data. Figure 3 shows different stages in the reconstruction process. We first apply levelART with a frequency of 10 MHz to this initial guess and run it for 30 sweeps. Then, we run levelART with 20 MHz for 30 more sweeps, and finally for another 30 sweeps with 30 MHz. The final reconstruction $\epsilon^{(N)}$ is shown in the lower right image of Figure 3. The final level set function $\phi^{(N)}$ corresponding to this reconstruction is displayed in Figure 14.

We see from this example that the shape reconstruction algorithm using level sets is able to split and merge boundaries easily in order to build up relatively complicated geometries. In the present situation, splitting and merging of boundaries was necessary for building the 'hole' in the reconstructed domain.

6.3 A cross-borehole situation with multiple objects

In our second numerical example, we consider a situation which is typical for geophysical applications. Comparable situations occur for example when we wish to monitor pollutant plumes at environmental cleanup sites from cross-borehole EM data.

We assume that we have 74 sources and receivers equidistantly distributed over two boreholes. The distance of the boreholes from each other is 10 meters, and the distance of two adjacent sources or receivers is 55 cm. The area between the two boreholes has to be monitored given the gathered data. The geometry is shown in Figure 4.

The background permittivity distribution in this example consists of four tilted layers with values of $\epsilon_b = 21$ in the top layer, and then continuing downwards with 20, 19, and again 21 for the deepest layer. The conductivity distribution σ_b is homogeneous with a value of $\sigma_b = 3.0 \times 10^{-4}$ S/m everywhere.

Embedded in this background are three compact inclusions as shown in Figure 4. The permittivity inside these inclusions is $\hat{\epsilon} = 5$, having a high contrast to the background values. The three inclusions are oriented such that there are two 'channels' of background material between them, one of them in the vertical and

one in the horizontal direction. The difficulty in this example is to separate the three inclusions from each other from the limited-view data. In particular, the reconstruction of the vertical channel is critical since we expect that the resolution in the horizontal direction will suffer from the missing data.

Again, we first apply the STAF reconstruction scheme to the data to get a first guess of the permittivity distribution $\epsilon^{(0)}$. Figure 5 shows the result for $G_s = \{30 \text{ MHz}\}$. Comparing this result with the reconstruction for the same frequency in our first numerical example, we conclude that the performance of STAF for high-frequency data is in the limited-view case not as good as in the case where we can use data with full view. We observe that the vertical resolution of the reconstruction is still good, whereas in the horizontal direction severe artifacts build up which reduce the quality of the high-frequency STAF reconstructions as an initial guess for levelART.

Figure 6 shows the corresponding STAF reconstruction using $G_s = \{5 \text{ MHz}\}$. We do not observe any artifacts in this reconstruction which might be caused by the limited view in the data. Therefore, we see that the decreased resolution of STAF using low-frequency data is in this situation compensated by a much higher robustness with respect to missing data. Keeping this in mind, we will typically start our reconstructions in the limited-view geometry by using the STAF result which correspond to (one or more of) the lowest available frequencies.

Starting out from the permittivity $\epsilon^{(0)}$ as shown in Figure 6, and the corresponding level set function $\phi^{(0)}$, we want to use the levelART algorithm in order to calculate a series of shape deformations which transforms the initial shape into the correct permittivity distribution. Figure 6 shows a reconstruction which uses data where the real part and the imaginary part have been contaminated by additive Gaussian noise with a signal-to-noise ratio (SNR) of 10 dB before starting the reconstruction process. Figure 7 shows the same reconstruction scheme, but with an even lower SNR of now 5 dB in the data.

Different strategies are possible for levelART. Which one works best, depends on the specific situation, for example the number and arrangement of sources and detectors, and on the noise level of the data. The strategy we use here (for both SNR values) is the following: First, we apply 20 steps of levelART with a frequency of 15 MHz to the initial guess. The result is shown in the lower left images of Figures 6 and 7. At this stage, the task of splitting the initial object into three subsets is almost completed.

Then, we apply levelART with a combination of three frequencies, namely 20, 25, and 30 MHz. This means that in a given sweep each of these three frequencies is used exactly once in the prescribed order, before starting again with the lowest frequency

(20 MHz) for the new sweep. This final step completes the reconstruction in just a few (about 10) sweeps. The succeeding sweeps do not improve the reconstruction significantly. Moreover, the norms of the residuals approach a constant value as the Figures 8 to 11 show.

Figures 8 to 11 show the evolution of the norms of the residuals during the reconstruction process for different signal-to-noise ratios in the data. The graphs with the symbol 'o' correspond to noiseless data, the graphs for a SNR of 10 dB are indicated by '*', and those for a SNR of 5 dB by '+'.

Figure 8 shows the norms of the residuals for $f = 15$ MHz during the 20 steps using the data with this frequency. The norms of the residuals decrease in all cases continually during the reconstruction process. Figures 9 to 11 show the evolution of the norms during the final 30 sweeps with the frequencies 20, 25 and 30 MHz. We see that after 10 sweeps the residuals approach some constant value which depends on the noise level of the data. In the lower right image of Figure 6, the reconstruction for a signal-to-noise ratio of 10 dB after completion of these 10 sweeps is shown. The corresponding level set function is shown in Figure 15.

Our experience is that marching over the higher frequencies in the described fashion stabilizes the inversion procedure especially in the limited-view situation considered here. However, so far we do not have any theoretical analysis which supports this observation.

Notice the artifacts which appear in the case of an extremely low SNR of 5 dB in Figure 7. These artifacts remain more or less stable when applying levelART with a constant frequency of 15 MHz, and disappear when marching to the higher frequencies in the succeeding reconstruction step. Notice that we also apply a diffusion ('curve shortening') filter for these higher frequencies, see section 4.10.

We observe again that levelART has no problems in propagating and tracking these multiple artifacts, even when they finally shrink and disappear. Notice also that, similar to the first numerical example, the algorithm splits the original boundary in order to arrive at the three separated inclusions forming the final reconstruction.

6.4 A cross-borehole situation with a single inclusion and variable conductivity

In our third numerical example, we want to test a situation where the conductivity inside the inclusions is different from the given background values. Since we did not take these conductivity changes into account when deriving the reconstruction algorithm, the question arises how much the performance of the reconstruction method will be effected by such changes in the conductivity distribution.

We assume therefore that we know the two values $\hat{\epsilon}$ and $\hat{\sigma}$ of the permittivity and the conductivity inside the inclusions, but both of them are different from the background values. We run the STAF routine as usual, which amounts to treating the conductivity changes simply as an additional form of noise. When applying levelART, we calculate the updates $\delta\phi^{(n)}$ for the level set function $\phi^{(n)}$ in the same way as derived above, but when determining the corresponding updated permittivity distribution $\epsilon^{(n)}$, we update at the same time the conductivity distribution $\sigma^{(n)}$ such that $\sigma(x) = \hat{\sigma}$ where the level set function $\phi^{(n)}$ has negative values. Strictly speaking, we still invert only for the permittivity ϵ , but we make use of the fact that inside the obstacles the conductivity and the permittivity are closely related to each other.

Figure 12 shows the geometry of this example, and Figure 13 shows the results for two different conductivity values $\hat{\sigma} = 1.0 \times 10^{-6}$ S/m and $\hat{\sigma} = 1.0 \times 10^{-2}$ S/m. Notice that these two values differ from each other and from the background value $\sigma_b = 3.0 \times 10^{-4}$ S/m by orders of magnitude! In both cases, Gaussian noise has been added to the real and imaginary parts of the data with a signal-to-noise ratio of 10 dB before starting the reconstruction routine.

As before, we start the reconstruction with the STAF guess corresponding to a frequency of 5 MHz. After only six sweeps of levelART, using the frequencies 15, 20, 25, and 30 MHz one after the other in each sweep, we arrive in both cases at a very good reconstruction of the permittivity distribution and of the conductivity distribution. We conclude that the performance of the reconstruction method (STAF and levelART) is not significantly effected by the changes in the conductivity distribution.

This robustness with respect to changes in the conductivity certainly has its limits. However, the example presented here makes us confident that in practical situations, when the conductivity value $\hat{\sigma}$ inside the obstacles is approximately known and not too large ($< 1.0 \times 10^{-2}$ S/m), the shape reconstruction method will perform stably and reliably and will give us a good reconstruction of the actual permittivity distribution.

7 Summary and future directions

We have presented a stable and efficient two-step shape reconstruction algorithm for EM cross-borehole tomography which uses adjoint fields and level sets. We have shown that this method is able to recover one or more objects with nontrivial shapes given noisy cross-borehole EM data.

The first step of this combined inversion scheme plays the role of an initializing procedure for the second step, and employs a 'source-type' inversion scheme to deal

with the high nonlinearity in the problem due to the presence of strong scatterers.

Although we believe that the preprocessing routine we propose here will work well in most situations, it can be replaced by any other preprocessing tool which shares the main features of the derived algorithm.

The second step of the inversion routine starts directly with the outcome of this initializing procedure, and continues by using a combination of an 'adjoint field technique' and a level set representation of the shapes until the inversion task is completed. We have shown that using a level set representation in this second step enables us to easily describe and keep track of complicated geometries which arise during the inversion process.

We mention that the FDFD routine, which has been employed in both steps to solve the forward and the adjoint Helmholtz problems, can be replaced by any other more efficient Helmholtz solver which has been tested to work reliably in the given situation.

We have shown in our numerical experiments that the proposed reconstruction scheme performs stably with respect to changes in the conductivity distribution, although these conductivity changes have not been taken into account for the derivation of the scheme. It would be desirable, however, to extend the reconstruction scheme to work simultaneously on the permittivity and the conductivity distribution. This seems to be possible, and we will address this problem in our future work.

We also assume that we know the permittivity values inside the obstacles, and that we only have to recover their shapes and their locations. In our future research, we will investigate the situation where both, the shapes and the permittivity values inside the obstacles, have to be recovered from the given data.

Throughout the paper, we have not clearly specified the degree of regularity which we require for the level set functions ϕ representing the domains Ω . A possible choice would be $\phi \in C_0^1(B_r(0))$ (i.e. continuously differentiable on $B_r(0)$ and zero on $\partial B_r(0)$), which would require some additional regularization in our numerical experiments. We also have introduced in (72) an approximated linearized operator $\Lambda'[\phi]$ motivated by our wish to use convenient inner products. Are there any function spaces which are more useful for our purposes? Will a practically useful reconstruction scheme result if we use different inner products instead of introducing $\Lambda'[\phi]$? To answer both questions, a thorough theoretical analysis has to be done to investigate the implications of using different function spaces for the level set representation.

The main ideas of the reconstruction method presented here are not restricted to a 2D geometry. Therefore, we believe that it is possible to extend the method to a more realistic 3D situation. All what is needed for this is an efficient forward

solver for the 3D system of Maxwell's equations. A forward solver which has been tested for such situations has been presented in [7, 18]. Moreover, applications to situations in medical imaging [2, 11], or in the nondestructive testing of materials [45], seem interesting and possible.

8 Acknowledgments

This work has been supported by a grant from the U. S. Dept. of Energy DE-FG07-97ID3566, by the Center for Subsurface Sensing and Imaging Systems at Northeastern University, by A CAREER Grant from the National Science Foundation MIP-9623721, and by The Army Research Office, Multidisciplinary University Research Initiative Grant No. DAAG55-97-0013.

9 Appendix

9.1 Proof of theorem 5.1

Green's formula for an infinite domain (without boundary terms since $\sigma > 0$) reads for general v, z

$$\begin{aligned} \int_{\mathbb{R}^2} [\Delta v + \kappa_k v] z \, dx + \int_{\mathbb{R}^2} v(x) \left(\sum_{d=1}^{D_j} \overline{\zeta_d} \delta(x - x_{jd}) \right) dx \\ = \int_{\mathbb{R}^2} v [\Delta z + \kappa_k z] \, dx + \sum_{d=1}^{D_j} \left(\int_{\mathbb{R}^2} v(x) \delta(x - x_{jd}) dx \right) \overline{\zeta_d} \end{aligned} \quad (106)$$

where we have used the notation $\kappa_k = a_k \epsilon_b + i b_k \sigma$. Let now v_{jk} be a solution of (77), and z_{jk} a solution of (82). Then the first term on the left hand side of (106) reads

$$\int_{\mathbb{R}^2} Q_{jk}^s(x) z_{jk}(x) \, dx = \left\langle Q_{jk}^s, \overline{z_{jk}} \chi_{B_r(0)} \right\rangle_Y, \quad (107)$$

whereas the second term on the right hand side is

$$\langle M_j v_{jk}, \zeta \rangle_{Z_j} = \left\langle A_{jk} Q_{jk}^s, \zeta \right\rangle_{Z_j}. \quad (108)$$

The remaining two terms cancel each other because of (82). Therefore, (106) gets the form

$$\left\langle Q_{jk}^s, \overline{z_{jk}} \chi_{B_r(0)} \right\rangle_Y = \left\langle A_{jk} Q_{jk}^s, \zeta \right\rangle_{Z_j}, \quad (109)$$

which proves the theorem.

9.2 Proof of theorem 5.2

Since $A_{jk}A_{jk}^*$ is a linear operator acting on the finite-dimensional data space, it is sufficient to find the action of $A_{jk}A_{jk}^*$ on each of the basis vectors $e_d = (0, \dots, 0, 1, 0, \dots, 0)^T$, $d = 1, \dots, D_j$, where the '1' is at the d -th position. From (83) we see that

$$\left(A_{jk}^* e_d\right)(x) = \overline{\varphi_{dk}(x)} \chi_{B_r(0)}(x). \quad (110)$$

Application of A_{jk} yields for the l -th component ($l = 1, \dots, D_j$)

$$\left(A_{jk}A_{jk}^* e_d\right)_l = v_{jk}(x_{jl}), \quad (111)$$

where v_{jk} is given by

$$v_{jk}(y) = \int_{B_r(0)} G_k(y, x) \overline{\varphi_{dk}(x)} dx \quad (112)$$

and $G_k(y, x)$ is Green's function satisfying

$$\Delta G_k(y, x) + (a_k \epsilon_b + i b_k \sigma) G_k(y, x) = \delta(y - x). \quad (113)$$

Reciprocity yields $G_k(x_{jl}, x) = \varphi_{lk}(x)$. Therefore, we get from (111), (112)

$$\left(A_{jk}A_{jk}^* e_d\right)_l = \int_{B_r(0)} \varphi_{lk}(x) \overline{\varphi_{dk}(x)} dx, \quad (114)$$

which proves the theorem.

References

- [1] Abdullah H and Louis A K 1999 The approximate inverse for solving an inverse scattering problem for acoustic waves in an inhomogeneous medium *Inverse Problems* **15** 1213-1229
- [2] Albanese R A, Medina R L and Penn J W 1994 Mathematics, medicine and microwaves *Inverse Problems* **10** 995-1007
- [3] Alumbaugh D L and Morrison H F 1995 Theoretical and practical considerations for crosswell electromagnetic tomography assuming a cylindrical geometry *Geophysics* **60** (3) 846-870
- [4] Angell T S, Kleinman R E and Roach F G 1987 An inverse transmission problem for the Helmholtz equation *Inverse Problems* **3** 149-80
- [5] Angell T S, Jiang X and Kleinman R E 1997 A distributed source method for inverse acoustic scattering *Inverse Problems* **13** 531-46
- [6] Caorsi S and Gragnani G L 1999 Inverse-scattering method for dielectric objects based on the reconstruction of the nonmeasurable equivalent current density *Radio Science* **34** (1) 1-8

- [7] Champagne N J, II, Berryman J G, Buettner H M, Grant J B and Sharpe R M 1999 A finite-difference frequency-domain code for electromagnetic induction tomography, in the *Proceedings of SAGEEP*, Oakland, CA, March 14–18, 931–940
- [8] Chen Y (1997) Inverse scattering via Heisenberg’s uncertainty principle *Inverse Problems* **13** 253-282
- [9] Chew W C, Wang Y M, Otto G, Lesselier D and Bolomey J Ch 1994 On the inverse source method of solving inverse scattering problems *Inverse Problems* **10** 547-553
- [10] Claerbout J F 1976 *Fundamentals of Geophysical Data Processing: With Applications to Petroleum Prospecting* McGraw-Hill, New York
- [11] Colton D and Monk P 1994 The detection and monitoring of leukemia using electromagnetic waves: mathematical theory *Inverse Problems* **10** 1235-1251
- [12] Colton D L and Kress R 1998 *Inverse Acoustic and Electromagnetic Scattering Theory* 2nd edn (Berlin: Springer)
- [13] Davis J L and Annan A P 1989 Ground penetrating radar for high resolution mapping of soil and rock stratigraphy *Geophys. Prospect.* **37** 531-51
- [14] Devaney A J and Sherman G C 1984 Nonuniqueness in inverse source and scattering problems *IEEE Trans. Antennas Propag.* **30** 1034-1037
- [15] Devaney A J 1986 Reconstructive tomography with diffracting wavefields *Inverse Problems* **2** 161-83
- [16] Dines K A and Lytle R J 1979 Computerized geophysical tomography *Proc. IEEE* **67** 1065–1073
- [17] Dorn O 1998 A transport-backtransport method for optical tomography *Inverse Problems* **14** 1107–1130
- [18] Dorn O, Bertete-Aguirre H, Berryman J G and Papanicolaou G C 1999 A nonlinear inversion method for 3D electromagnetic imaging using adjoint fields *Inverse Problems* **15** 1523-1558
- [19] Fisher E, McMechan G A and Annan A P 1992 Acquisition and processing of wide-aperture ground penetrating radar data *Geophysics* **57** 495-504
- [20] Habashy T M, Groom R W, Spies B R 1993 Beyond the Born and Rytov Approximations: A Nonlinear Approach to Electromagnetic Scattering *Journal of Geophysical Research* **98** (B2) 1759-1775
- [21] Habashy T M, Oristaglio M L and de Hoop A T 1994 Simultaneous nonlinear reconstruction of two-dimensional permittivity and conductivity *Radio Science* **29** (4) 1101-1118
- [22] Hettlich F 1995 Frechet derivatives in inverse obstacle scattering *Inverse Problems* **11** 371-382

- [23] Hettlich F and Rundell W 1997 Recovery of the support of a source term in an elliptic differential equation *Inverse Problems* **13** 959-976
- [24] Kaup P G, Santosa F and Vogelius M 1996 Method of imaging corrosion damage in thin plates from electrostatic data *Inverse Problems* **12** 279-93
- [25] Kilmer M, Miller E L and Rappaport C 1999 QMR-Based Projection Techniques for the Solution of Non-Hermitian Systems with Multiple Right Hand Sides, submitted to *SIAM Journal on Scientific and Statistical Computing*
- [26] Kolehmainen V, Arridge S R, Lionheart W R B, Vauhkonen M and Kaipio J P 1999 Recovery of region boundaries of piecewise constant coefficients of an elliptic PDE from boundary data *Inverse Problems* **15** 1375-1391
- [27] Ladas K T and Devaney A J 1992 Iterative methods in geophysical diffraction tomography *Inverse Problems* **8** 119-132
- [28] Litman A, Lesselier D and Santosa F 1998 Reconstruction of a two-dimensional binary obstacle by controlled evolution of a level-set *Inverse Problems* **14** 685-706
- [29] MATLAB: High-performance numeric computation and visualization software - Reference Guide 1992 *MathWorks* Natick MA
- [30] Miller E, Kilmer M and Rappaport C 1999 A New Shape-Based Method for Object Localization and Characterization from Scattered Field Data, submitted to *IEEE Trans. Geoscience and Remote Sensing*
- [31] Nachman A 1996 Global uniqueness for a two-dimensional inverse boundary value problem *Ann. Math.* **143** 71-96
- [32] Natterer F 1986 *The Mathematics of Computerized Tomography* (Stuttgart: Teubner)
- [33] Natterer F and Wübbeling F 1995 A propagation-backpropagation method for ultrasound tomography *Inverse Problems* **11** 1225-1232
- [34] Natterer F 1996 Numerical Solution of Bilinear Inverse Problems *Preprints* "Angewandte Mathematik und Informatik" 19/96-N Münster
- [35] Osher S and Sethian J 1988 Fronts propagation with curvature dependent speed: Algorithms based on Hamilton-Jacobi formulations *Journal of Computational Physics* **56** 12-49
- [36] Rappaport C M 1996 Interpreting and Improving the PML Absorbing Boundary Condition Using Anisotropic Lossy Mapping of Space *IEEE Transactions on Magnetism* **32** (3) 968-974
- [37] Rappaport C M, Kilmer M and Miller E 1999 Accuracy Considerations in Using the PML ABC with FDFD Helmholtz Equation Computation *Journal of Numerical Modelling* in press
- [38] Ramm A G 1986 *Scattering by obstacles* (Dordrecht: Reidel)

- [39] Rozier C, Lesselier D, Angell D and Kleinman R E 1996 Shape retrieval of an obstacle immersed in shallow water from single frequency fields using a complete family method *Inverse Problems* **13** 487-508
- [40] Santosa F 1996 A Level-Set Approach for Inverse Problems Involving Obstacles *ESAIM: Control, Optimization and Calculus of Variations* **1** 17-33
- [41] Sethian J A 1990 Numerical algorithms for propagating interfaces: Hamilton-Jacobi equations and conservation laws *J. Diff. Geom.* **31** 131-61
- [42] Sethian J A 1999 Level Set Methods and Fast Marching Methods (2nd ed) Cambridge University Press
- [43] Souriau L, B Duchene, Lesselier D and Kleinman R E 1996 Modified gradient approach to inverse scattering for binary objects in stratified media *Inverse Problems* **12** 463-481
- [44] Spies B P and Habashy T M 1995 Sensitivity analysis of crosswell electromagnetics *Geophysics* **60** 834-845
- [45] Special section on the conference on 'inverse problems, control and shape optimization' held 1998 in Carthage (Tunisia) 1999 *Inverse Problems* **15** (1) 1-134
- [46] Van den Berg P M and Kleinman R E 1997 A contrast source inversion method *Inverse Problems* **13** 1607-20
- [47] Van den Berg P M, van Broekhoven A L and Abubakar A 1999 Extended contrast source inversion *Inverse Problems* **15** 1325-1344
- [48] von Hippel A 1953 *Dielectric Materials and Applications* (Wiley: New York) 3-4
- [49] Ward S H and Hohmann G W 1987 Electromagnetic theory for geophysical applications, in *Electromagnetic Methods in Applied Geophysics – Theory*, Vol 1, Nabighian M N (ed.), SEG, Tulsa, Oklahoma 131-311
- [50] Wilt M J, Morrison H F, Becker A, Tseng H W, Lee K H, Torres-Verdin C, and Alumbaugh D 1995 Crosshole electromagnetic tomography: A new technology for oil field characterization, *The Leading Edge* **14** 173-177
- [51] Zhdanov M S, Traynin P and Booker J R 1996 Underground imaging by frequency-domain electromagnetic migration *Geophysics* **61**, 666-682

10 Figures

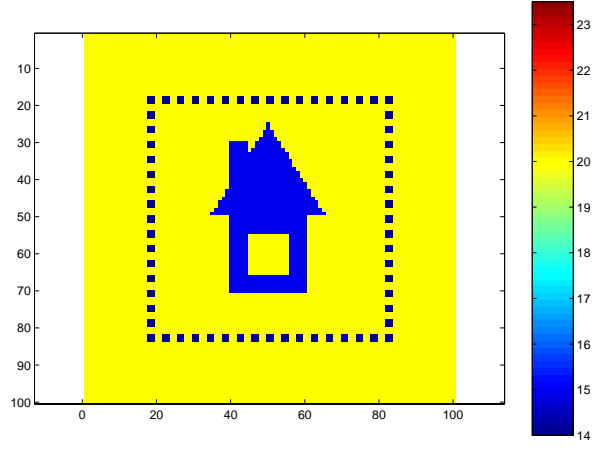


Figure 1: Original object for the example with full view. The dots in the figure indicate the source and receiver positions. The permittivity in the background is $\epsilon_b = 20$, and in the object $\hat{\epsilon} = 15$.

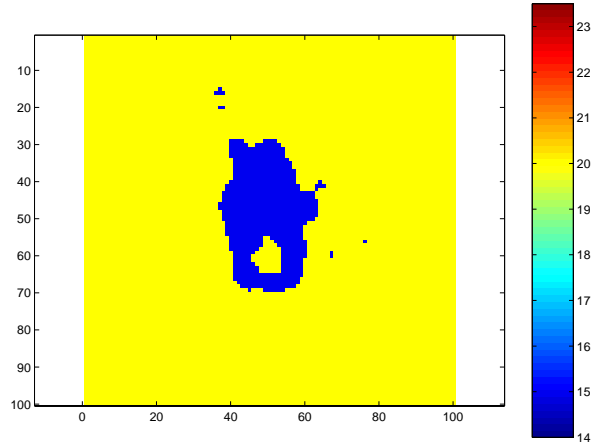


Figure 2: STAF reconstruction of permittivity distribution for the example with full view using $f = 30$ MHz and noisy data with 10 dB SNR.

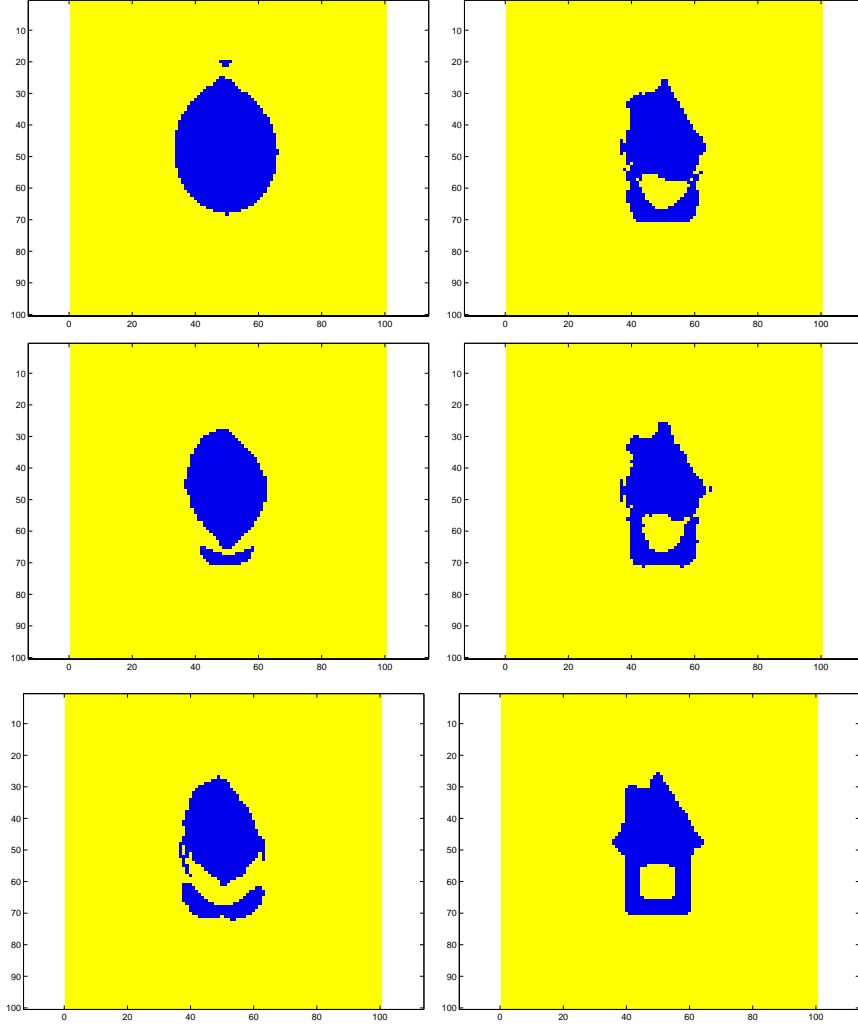


Figure 3: Evolution of permittivity $\epsilon^{(n)}$. Left column from top to bottom: STAF reconstructions of $\epsilon^{(0)}$ for 5 MHz (top left); This is the starting guess for the following reconstruction using levelART. After 10 steps of levelART with 10 MHz; After 30 steps with 10 MHz; Right column from top to bottom: After 10 steps with 20 MHz; After 30 steps with 20 MHz; Final reconstruction after 30 steps of levelART with 30 MHz (bottom right). The algorithm used noise-free data.

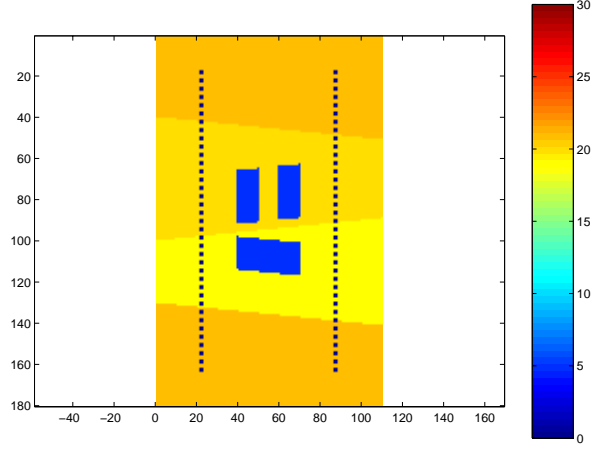


Figure 4: True permittivity distribution in the cross-borehole example. The dots in the figure indicate the source and receiver positions. The permittivity in the background layers is (from top to bottom) $\epsilon_b = 21, 20, 19$, and 21 . Inside the object it is $\hat{\epsilon} = 5$.

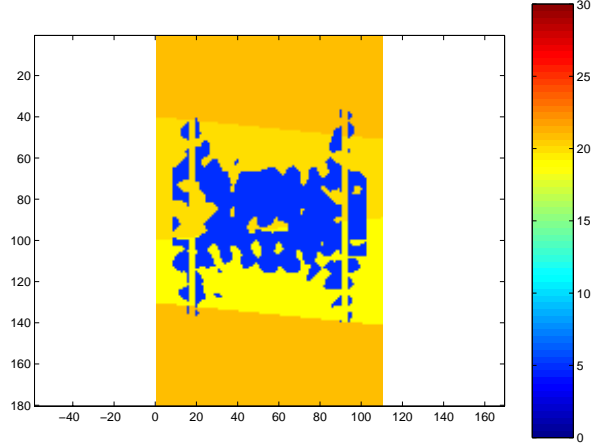


Figure 5: STAF reconstruction of permittivity distribution for cross-borehole example using noisy data with 30 MHz and 10 dB SNR.

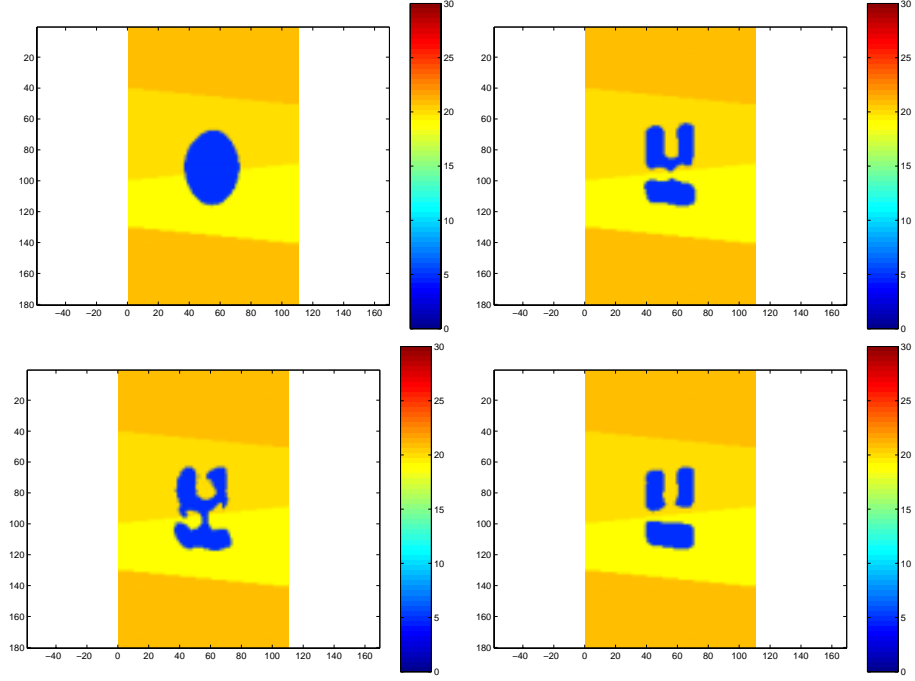


Figure 6: Evolution of the permittivity distribution $\epsilon^{(n)}$ in the cross-borehole example using noisy data with 10 dB SNR and limited view. Top left: STAF reconstruction of $\epsilon^{(0)}$ for 5 MHz. This is the starting guess for the following reconstruction using the levelART algorithm. Bottom left: After 20 steps of levelART with 15 MHz; Top right: After 2 sweeps with 20, 25, and 30 MHz; Bottom right: After 10 sweeps of levelART with 20, 25, and 30 MHz.

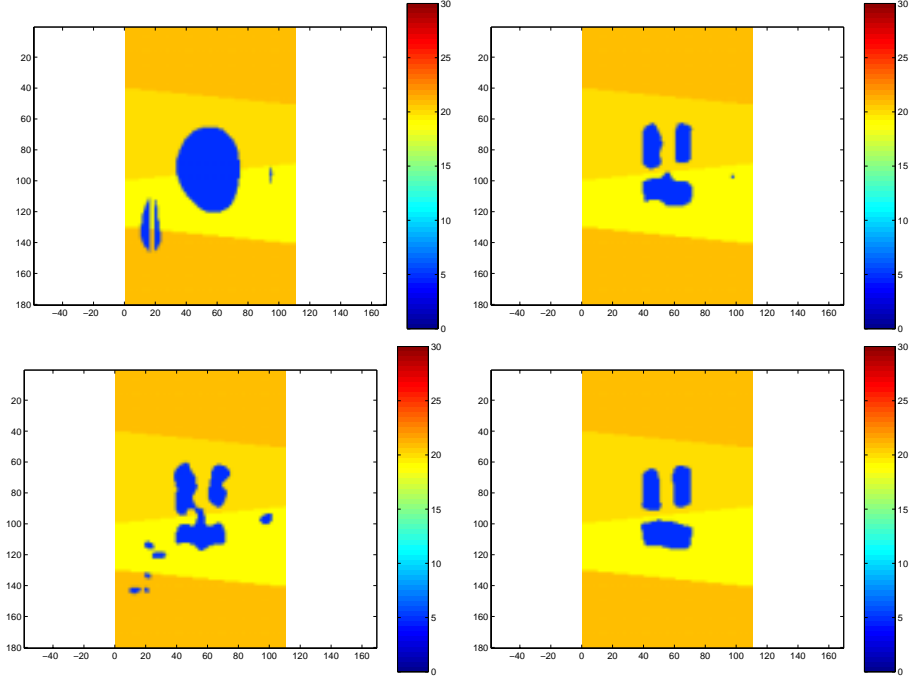


Figure 7: Evolution of the permittivity distribution $\epsilon^{(n)}$ in the cross-borehole example using noisy data with 5 dB SNR and limited view. Top left: STAF reconstruction of $\epsilon^{(0)}$ for 5 MHz. This is the starting guess for the following reconstruction using the levelART algorithm. Bottom left: After 20 steps of levelART with 15 MHz; Top right: After 2 sweeps with 20, 25, and 30 MHz; Bottom right: After 10 sweeps of levelART with 20, 25, and 30 MHz.

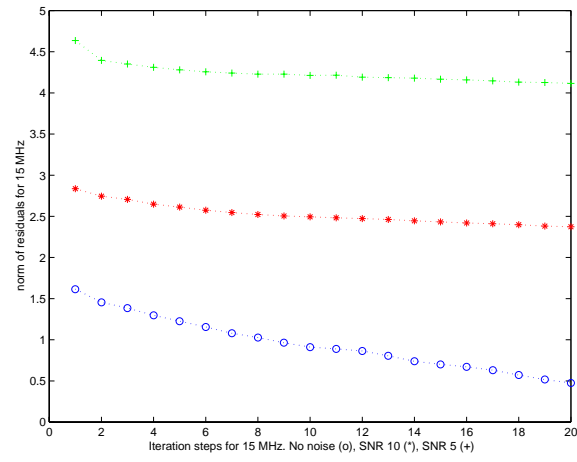


Figure 8: Norm of residuals for 15 MHz in cross-borehole example.

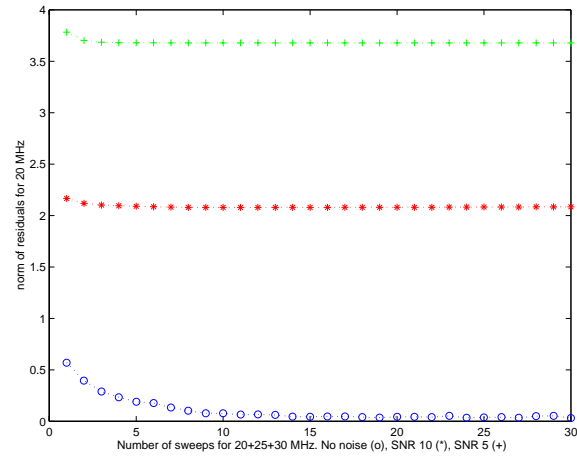


Figure 9: Norm of residuals for 20 MHz in cross-borehole example.

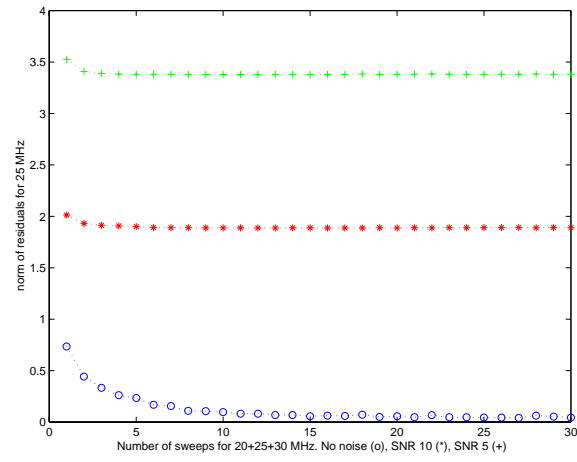


Figure 10: Norm of residuals for 25 MHz in cross-borehole example.

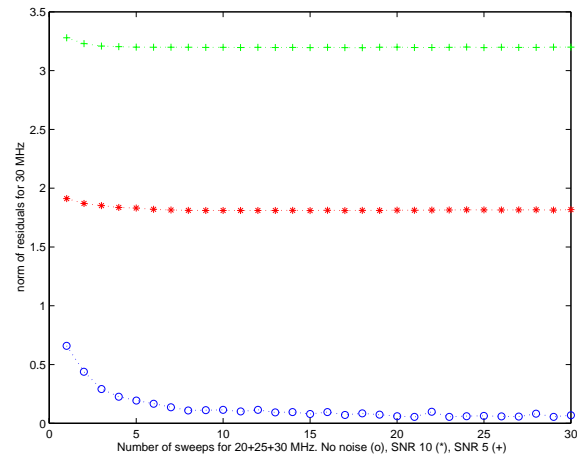


Figure 11: Norm of residuals for 30 MHz in cross-borehole example.

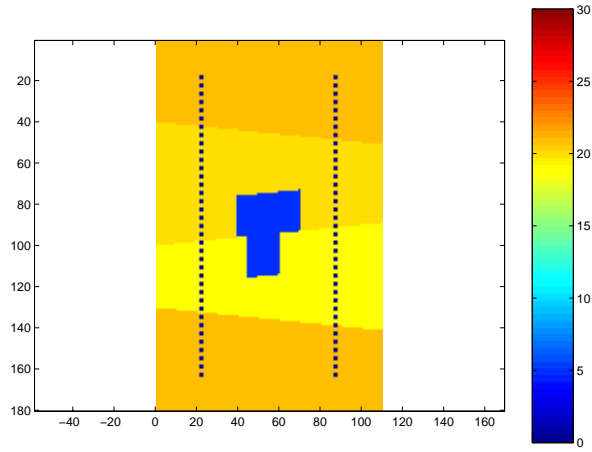


Figure 12: Original permittivity distribution $\epsilon^{(n)}$ in the cross-borehole example using noisy data with 10 dB SNR and limited view. The permittivity ϵ_b in the background is the same as in figure 4, and in the inclusion it is $\hat{\epsilon} = 5$. The conductivity in the background is $\sigma_b = 3.0 \times 10^{-4}$ S/m, and in the inclusion it is either $\hat{\sigma} = 1.0 \times 10^{-6}$ S/m (first example), or $\hat{\sigma} = 1.0 \times 10^{-2}$ S/m (second example). The dots in the figure indicate the source and receiver positions.

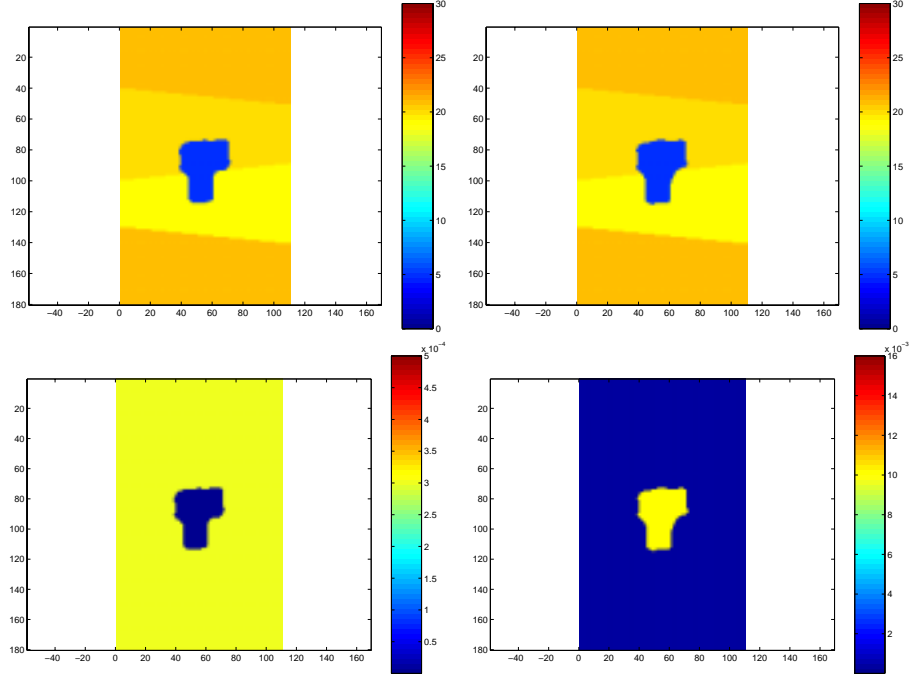


Figure 13: Reconstruction of permittivity and conductivity distributions after applying STAF with 5 MHz, and 6 sweeps of levelART with 15, 20, 25, and 30 MHz. Left column: Example with $\hat{\sigma} = 1.0 \times 10^{-6}$ S/m inside the obstacle. Shown is the reconstructed permittivity (top) and reconstructed conductivity (bottom). Right column: Example with $\hat{\sigma} = 1.0 \times 10^{-2}$ S/m inside the obstacle. Reconstructed permittivity (top) and reconstructed conductivity (bottom). The conductivity was treated as noise in STAF, and was considered linked to the current reconstruction of the permittivity distribution in levelART. All data were contaminated with white Gaussian noise of 10 dB SNR before starting the reconstruction process.

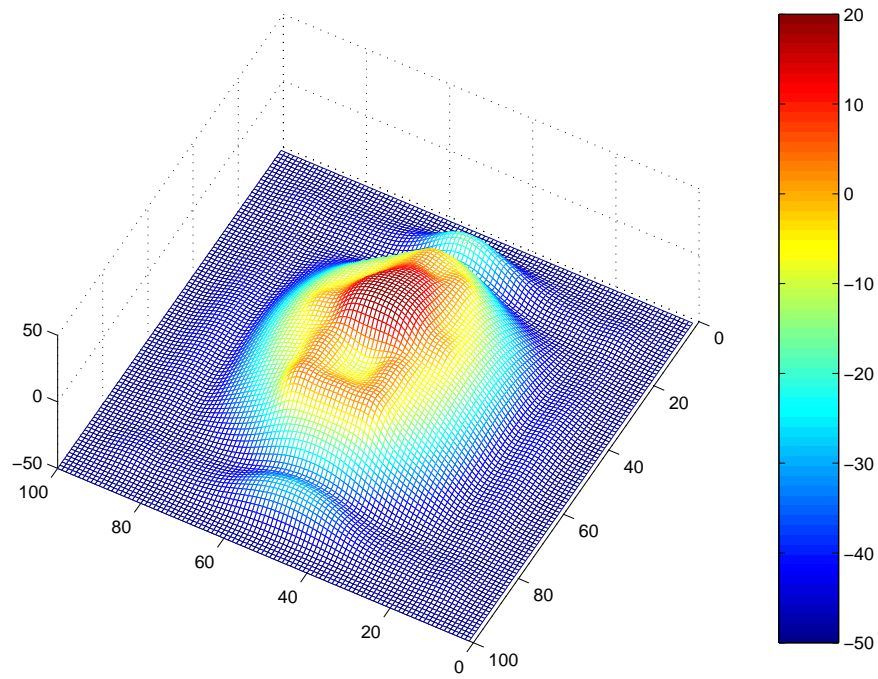


Figure 14: Final level set function $-\phi^{(N)}$ for the full-view example. Figure 3 shows the corresponding permittivity distribution $\epsilon^{(N)}$.

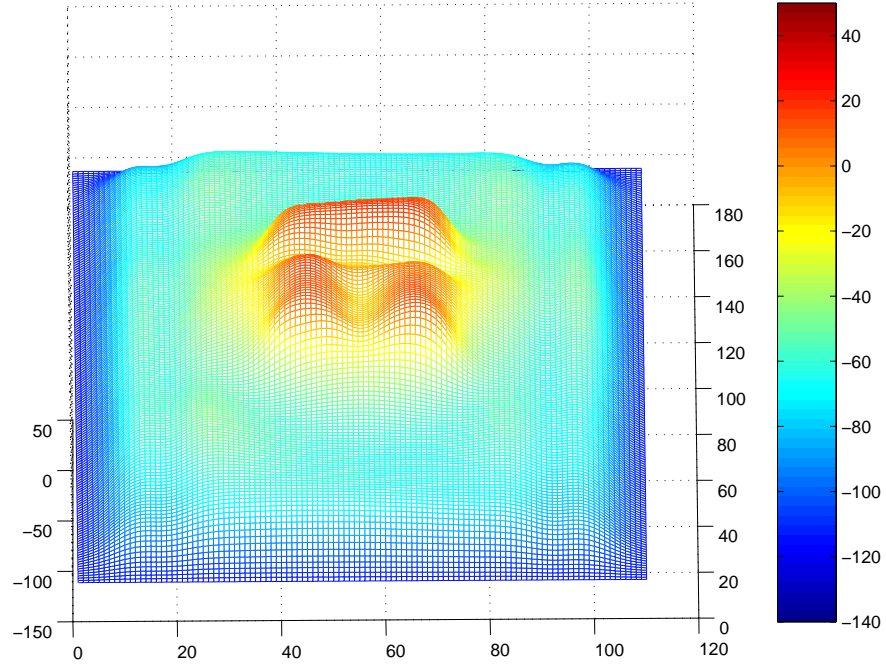


Figure 15: Final level set function $-\phi^{(N)}$ for the cross-borehole example using data with 10 dB SNR. Figure 6 shows the corresponding permittivity distribution $\epsilon^{(N)}$.